LBNL-50088
Preprint

ERNEST ORLANDO LAWRENCE BERKELEY NATIONAL LABORATORY

Applications of Plane-Wave Destruction Filters

Sergey Fomel

Computing Sciences Directorate
Mathematics Department

April 2002

Submitted to
Geophysics

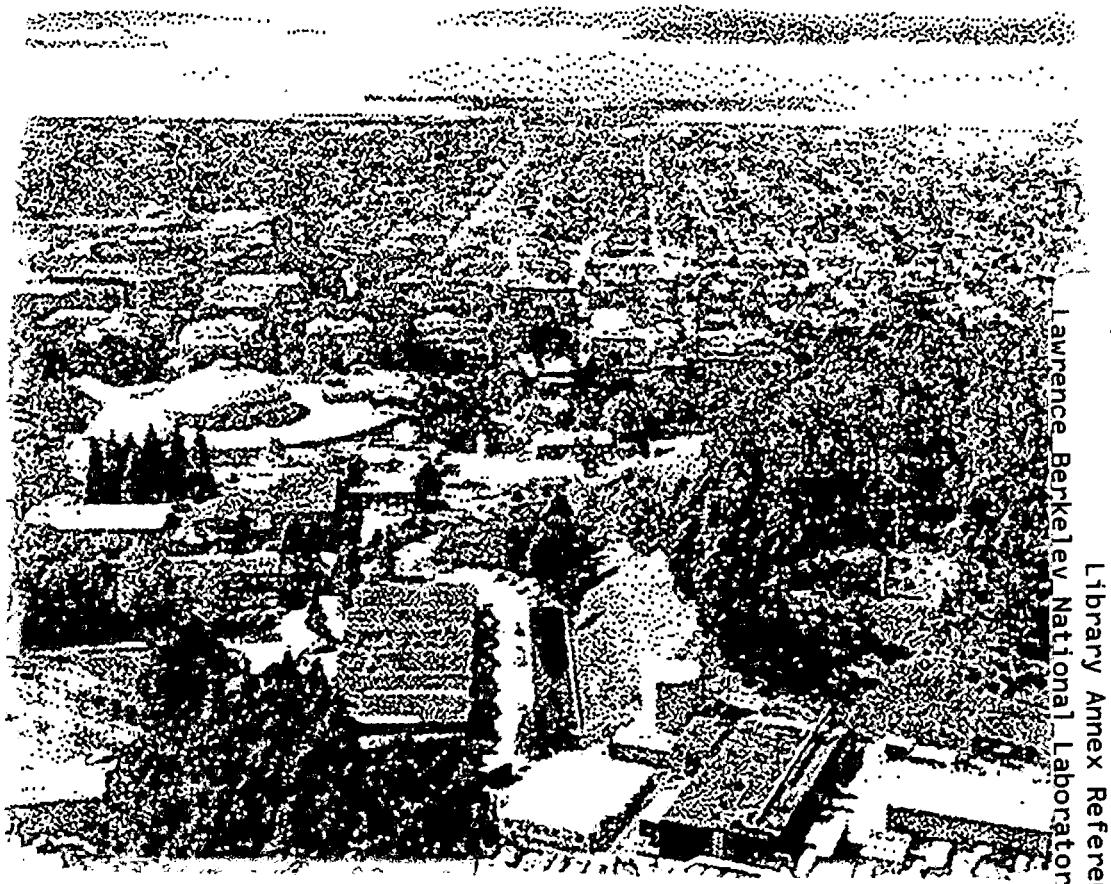

REFERENCE COPY
Does Not
Circulate
Library Annex Reference
Lawrence Berkeley National Laboratory
Copy 1

DISCLAIMER

This document was prepared as an account of work sponsored by the United States Government. While this document is believed to contain correct information, neither the United States Government nor any agency thereof, nor The Regents of the University of California, nor any of their employees, makes any warranty, express or implied, or assumes any legal responsibility for the accuracy, completeness, or usefulness of any information, apparatus, product, or process disclosed, or represents that its use would not infringe privately owned rights. Reference herein to any specific commercial product, process, or service by its trade name, trademark, manufacturer, or otherwise, does not necessarily constitute or imply its endorsement, recommendation, or favoring by the United States Government or any agency thereof, or The Regents of the University of California. The views and opinions of authors expressed herein do not necessarily state or reflect those of the United States Government or any agency thereof, or The Regents of the University of California.

Ernest Orlando Lawrence Berkeley National Laboratory
is an equal opportunity employer.

DISCLAIMER

This document was prepared as an account of work sponsored by the United States Government. While this document is believed to contain correct information, neither the United States Government nor any agency thereof, nor the Regents of the University of California, nor any of their employees, makes any warranty, express or implied, or assumes any legal responsibility for the accuracy, completeness, or usefulness of any information, apparatus, product, or process disclosed, or represents that its use would not infringe privately owned rights. Reference herein to any specific commercial product, process, or service by its trade name, trademark, manufacturer, or otherwise, does not necessarily constitute or imply its endorsement, recommendation, or favoring by the United States Government or any agency thereof, or the Regents of the University of California. The views and opinions of authors expressed herein do not necessarily state or reflect those of the United States Government or any agency thereof or the Regents of the University of California.

LBNL-50088

Applications of Plane-Wave Destruction Filters

Sergey Fomel

Computing Sciences Directorate
Mathematics Department
Ernest Orlando Lawrence Berkeley National Laboratory
University of California
Berkeley, California 94720

April 2002

This work was supported by the Director, Office of Science, Office of Advanced Scientific Computing Research, Mathematical, Information, and Computational Sciences Division, of the U.S. Department of Energy under Contract No. DE-AC03-76SF00098.

Applications of plane-wave destruction filters[a]

[a]Accepted for publication in *Geophysics*

Sergey Fomel

Lawrence Berkeley National Laboratory,

1 Cyclotron Road, Mail Stop 50A-1148,

Berkeley, CA 94720,

(April 5, 2002)

ABSTRACT

Plane-wave destruction filters originate from a local plane-wave model for characterizing seismic data. These filters can be thought of as a T-X analog of F-X prediction-error filters and as an alternative to T-X prediction-error filters. The filters are constructed with the help of an implicit finite-difference scheme for the local plane-wave equation. On several synthetic and real-data examples, I demonstrate that finite-difference plane-wave destruction filters perform well in applications such as fault detection, data interpolation, and noise attenuation.

INTRODUCTION

Plane-wave destruction filters, introduced by Claerbout (1992), serve the purpose of characterizing seismic images by a superposition of local plane waves. They are constructed as finite-difference stencils for the plane-wave differential equation. In many cases, a local plane-wave model is a very convenient representation of seismic data. Unfortunately, early experiences with applying plane-wave destructors for interpolating spatially aliased data (Nichols, 1990; Claerbout, 1992) demonstrated their poor performance in comparison with that of industry-standard F-X prediction-error filters (Spitz, 1991).

For each given frequency, an F-X prediction-error filter (PEF) can be thought of as a Z-transform polynomial. The roots of the polynomial correspond precisely to predicted plane waves (Canales, 1984). Therefore, F-X PEFs simply represent a spectral (frequency-domain) approach to plane-wave destruction[1] This powerful and efficient approach is, however, not theoretically adequate when the plane-wave slopes or the boundary conditions vary both spatially and temporally. In practice, this limitation is addressed by breaking the data into windows and assuming that the slopes are stationary within each window.

Multidimensional T-X prediction-error filters (Claerbout, 1992, 1999) share the same purpose of predicting local plane waves. They work well with spatially aliased data and allow for both temporal and spatial variability of the slopes. In practice, however, T-X filters appear as very mysterious objects, because their construction involves many non-intuitive parameters. The user needs to choose a raft of parameters, such as the number of filter coefficients, the gap and the exact shape of the filter, the size, number, and shape of local patches for filter estimation, the number

[1]The filters are designed to *destruct* local plane waves. However, in applications such as data interpolation, they are often used to *reconstruct* the missing parts of local waves. The choice of terminology should not confuse the reader.

of iterations, and the amount of regularization. Recently developed techniques for handling non-stationary PEFs (Crawley et al., 1999) performed well in a variety of applications (Crawley, 2000; Guitton et al., 2001), but the large number of adjustable parameters still requires a significant level of human interaction and remains the drawback of the method.

Clapp et al. (1998) have recently revived the original plane-wave destructors for preconditioning tomographic problems with a predefined dip field (Clapp, 2000). The filters were named *steering filters* because of their ability to steer the solution in the direction of the local dips. The name is also reminiscent of *steerable filters* used in medical image processing (Freeman and Adelson, 1991; Simoncelli and Farid, 1996).

In this paper, I revisit Claerbout's original technique of finite-difference plane-wave destruction. First, I develop an approach for increasing the accuracy and dip bandwidth of the method. Applying the improved filter design to several data regularization problems, I discover that the finite-difference filters often perform as well as, or even better than, T-X PEFs. At the same time, they keep the number of adjustable parameters to a minimum, and the only estimated quantity has a clear physical meaning of the local plane-wave slope. No local windows are required, because the slope is estimated as a smoothly variable continuous function of the data coordinates.

Conventional methods for estimating plane-wave slopes are based on picking maximum values of stacking semblance and other cumulative coherency measures (Neidell and Taner, 1971). The differential approach to slope estimation, employed by plane-wave destruction filters, is related to the differential semblance method (Symes and Carazzone, 1991). Its theoretical superiority to conventional semblance measures for the problem of local plane wave detection has been established by Symes (1994) and Kim and Symes (1998).

HIGH-ORDER PLANE-WAVE DESTRUCTORS

Following the physical model of local plane waves, we can define the mathematical basis of the plane-wave destruction filters as the local plane differential equation

$$\frac{\partial P}{\partial x} + \sigma \frac{\partial P}{\partial t} = 0 \,, \tag{1}$$

where $P(t,x)$ is the wave field, and σ is the local slope, which may also depend on t and x. In the case of a constant slope, equation (1) has the simple general solution

$$P(t,x) = f(t - \sigma x) \,, \tag{2}$$

where $f(t)$ is an arbitrary waveform. Equation (2) is nothing more than a mathematical description of a plane wave.

If we assume that the slope σ does not depend on t, we can transform equation (1) to the frequency domain, where it takes the form of the ordinary differential equation

$$\frac{d\hat{P}}{dx} + i\omega\sigma\hat{P} = 0 \tag{3}$$

and has the general solution

$$\hat{P}(x) = \hat{P}(0)\, e^{i\omega\sigma x} \,, \tag{4}$$

where $\hat{P}$ is the Fourier transform of P. The complex exponential term in equation (4) simply represents a shift of a t-trace according to the slope σ and the trace separation x.

In the frequency domain, the operator for transforming the trace at position $x-1$ to the neighboring trace[2] and at position x is a multiplication by $e^{i\omega\sigma}$. In other words, a plane wave can be perfectly predicted by a two-term prediction-error filter in the F-X domain:

$$a_0\,\hat{P}(x) + a_1\,\hat{P}(x-1) = 0 \,, \tag{5}$$

[2]For simplicity, it is assumed that x takes integer values that correspond to trace numbering.

where $a_0 = 1$ and $a_1 = -e^{i\omega\sigma}$. The goal of predicting several plane waves can be accomplished by cascading several two-term filters. In fact, any F-X prediction-error filter represented in the Z-transform notation as

$$A(Z_x) = 1 + a_1 Z_x + a_2 Z_x^2 + \cdots + a_N Z_x^N \tag{6}$$

can be factored into a product of two-term filters:

$$A(Z_x) = \left(1 - \frac{Z_x}{Z_1}\right)\left(1 - \frac{Z_x}{Z_2}\right)\cdots\left(1 - \frac{Z_x}{Z_N}\right), \tag{7}$$

where $Z_1, Z_2, \ldots, Z_N$ are the zeroes of polynomial (6). According to equation (5), the phase of each zero corresponds to the slope of a local plane wave multiplied by the frequency. Zeroes that are not on the unit circle carry an additional amplitude gain not included in equation (3).

In order to incorporate time-varying slopes, we need to return to the time domain and look for an appropriate analog of the phase-shift operator (4) and the plane-prediction filter (5). An important property of plane-wave propagation across different traces is that the total energy of the propagating wave stays invariant throughout the process: the energy of the wave at one trace is completely transmitted to the next trace. This property is assured in the frequency-domain solution (4) by the fact that the spectrum of the complex exponential $e^{i\omega\sigma}$ is equal to one. In the time domain, we can reach an equivalent effect by using an all-pass digital filter. In the Z-transform notation, convolution with an all-pass filter takes the form

$$\hat{P}_{x+1}(Z_t) = \hat{P}_x(Z_t)\frac{B(Z_t)}{B(1/Z_t)}, \tag{8}$$

where $\hat{P}_x(Z_t)$ denotes the Z-transform of the corresponding trace, and the ratio $B(Z_t)/B(1/Z_t)$ is an all-pass digital filter approximating the time-shift operator $e^{i\omega\sigma}$. In finite-difference terms, equation (8) represents an implicit finite-difference scheme for solving equation (1) with the initial conditions at a constant x. The coefficients of filter $B(Z_t)$ can be determined, for example, by fitting the

filter frequency response at low frequencies to the response of the phase-shift operator. The Taylor series technique (equating the coefficients of the Taylor series expansion around zero frequency) yields the expression

$$B_3(Z_t) = \frac{(1-\sigma)(2-\sigma)}{12} Z_t^{-1} + \frac{(2+\sigma)(2-\sigma)}{6} + \frac{(1+\sigma)(2+\sigma)}{12} Z_t \tag{9}$$

for a three-point centered filter $B_3(Z_t)$ and the expression

$$\begin{aligned} B_5(Z_t) \;=\; & \frac{(1-\sigma)(2-\sigma)(3-\sigma)(4-\sigma)}{1680} Z_t^{-2} + \frac{(4-\sigma)(2-\sigma)(3-\sigma)(4+\sigma)}{420} Z_t^{-1} + \\ & \frac{(4-\sigma)(3-\sigma)(3+\sigma)(4+\sigma)}{280} + \\ & \frac{(4-\sigma)(2+\sigma)(3+\sigma)(4+\sigma)}{420} Z_t + \frac{(1+\sigma)(2+\sigma)(3+\sigma)(4+\sigma)}{1680} Z_t^2 \end{aligned} \tag{10}$$

for a five-point centered filter $B_5(Z_t)$. The derivation of equations (9-10) is detailed in the appendix. It is easy to generalize these equations to longer filters. Figure 1 shows the phase of the all-pass filters $B_3(Z_t)/B_3(1/Z_t)$ and $B_5(Z_t)/B_5(1/Z_t)$ for two values of the slope σ in comparison with the exact linear function of equation (4). As expected, the phases match the exact line at low frequencies, and the accuracy of the approximation increases with the length of the filter.

Taking both dimensions into consideration, equation (8) transforms to the prediction equation analogous to (5) with the 2-D prediction filter

$$A(Z_t, Z_x) = 1 - Z_x \frac{B(Z_t)}{B(1/Z_t)} \,. \tag{11}$$

In order to characterize several plane waves, we can cascade several filters of the form (11) in a manner similar to that of equation (7). In the examples of this paper, I use a modified version of the filter $A(Z_t, Z_x)$, namely the filter

$$C(Z_t, Z_x) = A(Z_t, Z_x) B(1/Z_t) = B(1/Z_t) - Z_x B(Z_t) \,, \tag{12}$$

which avoids the need for polynomial division. In case of the 3-point filter (9), the 2-D filter (12) has exactly six coefficients. It consists of two columns, each column having three coefficients and

the second column being a reversed copy of the first one. When filter (12) is used in data regularization problems, it can occasionally cause undesired high-frequency oscillations in the solution, resulting from the near-Nyquist zeroes of the polynomial $B(Z_t)$. The oscillations are easily removed in practice with appropriate low-pass filtering.

In the next section, I address the problem of estimating the local slope σ with filters of form (12). Estimating the slope is a necessary step for applying the finite-difference plane-wave filters on real data.

SLOPE ESTIMATION

Let us denote by $\mathbf{C}(\sigma)$ the operator of convolving the data with the 2-D filter $C(Z_t, Z_x)$ of equation (12), assuming the local slope σ is known. In order to determine the slope, we can define the least-squares goal

$$\mathbf{C}(\sigma)\mathbf{d} \approx 0\,, \tag{13}$$

where $\mathbf{d}$ is the known data and the approximate equality implies that the solution is found by minimizing the power of the left-hand side. Equations (9) and (10) show that the slope σ enters in the filter coefficients in an essentially non-linear way. However, one can still apply the linear iterative optimization methods by an analytical linearization of equation (13). The linearization (also known as the Gauss-Newton iteration) implies solving the linear system

$$\mathbf{C}'(\sigma_0)\Delta\sigma\mathbf{d} + \mathbf{C}(\sigma_0)\mathbf{d} \approx 0 \tag{14}$$

for the slope increment $\Delta\sigma$. Here σ_0 is the initial slope estimate, and $\mathbf{C}'(\sigma)$ is a convolution with the filter, obtained by differentiating the filter coefficients of $\mathbf{C}(\sigma)$ with respect to σ. After system (14) is solved, the initial slope σ_0 is updated by adding $\Delta\sigma$ to it, and one can solve the linear problem

again. Depending on the starting solution, the method may require several non-linear iterations to achieve an acceptable convergence.

The slope σ in equation (14) does not have to be constant. We can consider it as varying in both time and space coordinates. This eliminates the need for local windows but may lead to undesirably rough (oscillatory) local slope estimates. Moreover, the solution will be undefined in regions of unknown or constant data, because for these regions the local slope is not constrained. Both these problems are solved by adding a regularization (styling) goal to system (14). The additional goal takes the form

$$\varepsilon \mathbf{D} \Delta\sigma \approx 0 \,, \tag{15}$$

where $\mathbf{D}$ is an appropriate roughening operator and ε is a scaling coefficient. For simplicity, I chose $\mathbf{D}$ to be the gradient operator. More efficient and sophisticated helical preconditioning techniques are available (Claerbout, 1998; Fomel, 2000; Fomel and Claerbout, 2001).

In theory, estimating two different slopes σ_1 and σ_2 from the available data is only marginally more complicated than estimating a single slope. The convolution operator becomes a cascade of $\mathbf{C}(\sigma_1)$ and $\mathbf{C}(\sigma_2)$, and the linearization yields

$$\mathbf{C}'(\sigma_1)\mathbf{C}(\sigma_2)\Delta\sigma_1 \mathbf{d} + \mathbf{C}(\sigma_1)\mathbf{C}'(\sigma_2)\Delta\sigma_2 \mathbf{d} + \mathbf{C}(\sigma_1)\mathbf{C}(\sigma_2)\mathbf{d} \approx 0 \,. \tag{16}$$

The regularization condition should now be applied to both $\Delta\sigma_1$ and $\Delta\sigma_2$:

$$\varepsilon \mathbf{D} \Delta\sigma_1 \approx 0 \,; \tag{17}$$

$$\varepsilon \mathbf{D} \Delta\sigma_2 \approx 0 \,. \tag{18}$$

The solution will obviously depend on the initial values of σ_1 and σ_2, which should not be equal to each other. System (16) is generally underdetermined, because it contains twice as many estimated parameters as equations: The number of equations corresponds to the grid size of the data $\mathbf{d}$, while

characterizing variable slopes σ_1 and σ_2 on the same grid involves two gridded functions. However, an appropriate choice of the starting solution and the additional regularization (17-18) allow us to arrive at a practical solution.

The application examples of the next section demonstrate that when the system of equations (14-15) or (16-18) are optimized in the least-squares sense in a cycle of several linearization iterations, it leads to smooth and reliable slope estimates. The regularization conditions (15) and (17-18) assure a smooth extrapolation of the slope to the regions of unknown or constant data.

APPLICATION EXAMPLES

In this section, I examine the performance of the finite-difference plane-destruction filters on several test applications. The general framework for applying these filters consists of the two steps:

1. Estimate the dominant local slope (or a set of local slopes) from the data. This step follows the least-squares optimization embedded in equations (14) or (16). Thanks to the general regularization technique of equations (15) and (17-18), locally smooth slope estimates are obtained without any need for breaking the data into local windows. Of course, local windows can be employed for other purposes (parallelization, memory management, etc.) Selecting appropriate initial values for the local slopes can speed up the computation and steer it towards desirable results. It is easy to incorporate additional constraints on the local slope values.

2. Using the estimated slope, apply non-stationary plane-wave destruction filters for the particular application purposes. In the fault detection application, we simply look at the output of plane-wave destruction. In the interpolation application, the filters are used to constrain the missing data. In the noise attenuation application, they characterize the coherent signal and noise components in the data.

A description of these particular applications follows next.

Fault detection

The use of prediction-error filters in the problem of detecting local discontinuities was suggested by Claerbout (1994, 1999), and further refined by Schwab et al. (1996) and Schwab (1998). Bednar (1998) used simple plane-destruction filters in a similar setting to compute coherency attributes.

To test the performance of the improved plane-wave destructors, I chose several examples from Claerbout (1999). Figure 2 introduces the first example. The left plot of the figure shows a synthetic model, which resembles sedimentary layers with a plane unconformity and a curvilinear fault. The model contains 200 traces of 200 samples each. The right plot shows the corresponding *texture* (Claerbout and Brown, 1999), obtained by convolving a field of random numbers with the inverse of plane-wave destruction filters. The inverses are constructed using helical filtering techniques (Claerbout, 1998; Fomel, 2000). Texture plots allow us to quickly access the ability of the destruction filters to characterize the main locally plane features in the data. The dip field was estimated by the linearization method of the previous section. The dip field itself and the prediction residual [the left-hand side of equation (13)] are shown in the left and right plots of Figure 3 respectively. We observe that the texture plot does reflect the dip structure of the input data, which indicates that the dip field was estimated correctly. The fault and unconformity are clearly visible both in the dip estimate and in the residual plots. Anywhere outside the slope discontinuities and the boundaries, the residual is close to zero. Therefore, it can be used directly as a fault detection measure. Comparing the residual plot in Figure 3 with the analogous plot of Claerbout (1994, 1999), reproduced in Figure 4, establishes a superior performance of the improved finite-difference destructors in comparison with that of the local T-X prediction-error filters.

The left plot in Figure 5 introduces a simpler synthetic test. The model is composed of linear events with two conflicting slopes. A regularized dip field estimation attempts to smooth the estimated dip in the places where it is not constrained by the data (the left plot of Figure 6.) The effect of smoothing is clearly seen in the texture image (the right plot in Figure 5). The corresponding residual (the right plot of Figure 6) shows suppressed linear events and highlights the places of their intersection. Residuals are large at intersections because a single dominant dip model fails to adequately represent both conflicting dips.

The left plot in Figure 7 shows a real shot gather: a portion of Yilmaz and Cumro (1983) data set 27. The initial dip in the dip estimation program was set to zero. Therefore, the texture image (the right plot in Figure 7) contains zero-dipping plane waves in the places of no data. Everywhere else the dip is accurately estimated from the data. The data contain a missing trace at about 0.7 km offset and a slightly shifted (possibly mispositioned) trace at about 1.1 km offset. The mispositioned trace is clearly visible in the dip estimate (the left plot in Figure 8), and the missing trace is emphasized in the residual image (the right plot in Figure 8). Additionally, the residual image reveals the forward and back-scattered surface waves, hidden under more energetic reflections in the input data.

Figure 9 shows a stacked time section from the Gulf of Mexico and its corresponding texture. The texture plot demonstrates that the estimated dip (the left plot of Figure 10) reflects the dominant local dip in the data. After the plane waves with the dominant dip are removed, many hidden diffractions appear in the residual image (the right plot in Figure 10.) The enhanced diffraction events can be used, for example, for estimating the medium velocity (Harlan et al., 1984).

Overall, the examples of this subsection show that the finite-difference plane-wave destructors provide a reliable tool for enhancement of discontinuities and conflicting slopes in seismic images. The estimation step of the fault detection procedure produces an image of the local dominant dip

field, which may have its own interpretational value. An extension to 3-D is possible, as outlined by Schwab (1998), Clapp (2000), and Fomel (2000).

Trace interpolation beyond aliasing

Spitz (1991) popularized the application of prediction-error filters to regular trace interpolation and showed how the spatial aliasing restriction can be overcome by scaling the lower frequencies of F-X PEFs. An analogous technique for T-X filters was developed by Claerbout (1992, 1999) and was applied for 3-D interpolation with non-stationary PEFs by Crawley (2000). The T-X technique implies stretching the filter in all directions so that its dip spectrum is preserved while the coefficients are estimated at alternating traces. After the filter is estimated, it is scaled back and used for interpolating missing traces between the known ones. A very similar method works for finite-difference plane wave destructors, only we need to take special care of the aliased dips at the dip estimation stage.

A simple synthetic example of interpolation beyond aliasing is shown in Figure 11. The input data are clearly aliased and non-stationary. To take the aliasing into account, I estimate the two dips present in the data with the slope estimation technique of equations (16) and (17-18). The first dip corresponds to the true slope, while the second dip corresponds to the aliased dip component. In this example, the true dip is non-negative everywhere and is easily distinguished from the aliased one. In the more general case, an additional interpretation may be required to determine which of the dip components is contaminated by aliasing. Throwing away the aliased dip and interpolating intermediate traces with the true dip produces the accurate interpolation result shown in the right plot of Figure 11. Three additional traces were inserted between each of the neighboring input traces.

Figure 12 shows a marine 2-D shot gather from a deep water Gulf of Mexico survey before and after subsampling in the offset direction. The data are similar to those used by Crawley (2000). The shot gather has long-period multiples and complicated diffraction events caused by a salt body. The amplitudes of the hyperbolic events are not as uniformly distributed as in the synthetic case of Figure 11. Subsampling by a factor of two (the right plot in Figure 12) causes clearly visible aliasing in the steeply dipping events. The goal of the experiment is to interpolate the missing traces in the subsampled data and to compare the result with the original gather shown in the left plot of Figure 12.

A straightforward application of the dip estimation equations (16-18) applied to aliased data can easily lead to erroneous aliased dip estimation because the aliased dip may get picked instead of the true dip. In order to avoid this problem, I chose a slightly more complex strategy. The algorithm for trace interpolation of aliased data consists of the following steps:

1. Applying Claerbout's T-X methodology, stretch a two-dip plane-wave destruction filter and estimate the dips from decimated data.

2. The second estimated dip will be degraded by aliasing. Ignore this initial second-dip estimate.

3. Estimate the second dip component again by fixing the first dip component and using it as the initial estimate of the second component. This trick prevents the nonlinear estimation algorithm from picking the wrong (aliased) dip in the data.

4. Downscale the estimated two-dip filter and use it for interpolating missing traces.

The two estimated dip components are shown in Figure 13. The first component contains only positive dips. The second component coincides with the first one in the areas where only a single dip is present in the data. In other areas, it picks the complementary dip, which has a negative value

for back-dipping hyperbolic diffractions.

Figure 14 shows the interpolation result and the difference between the interpolated traces and the original traces, plotted at the same clip value. The method succeeded in the sense that it is impossible to distinguish interpolated traces from the interpolation result alone. However, it is not ideal, because some of the original energy is missing in the output. A close-up comparison between the original and the interpolated traces in Figure 15 shows that imperfection in more detail. Some of the steepest events in the middle of the section are poorly interpolated, and in some of the other places, the second dip component is continued instead of the first one.

One could improve the interpolation result considerably by including another dimension. To achieve a better result, we can use a pair of plane-wave destructors, one predicting local plane waves in the offset direction and the other predicting local plane waves in the shot direction.

Signal and noise separation

Signal and noise separation and noise attenuation are yet another important application of plane-wave prediction filters. A random noise attention has been successfully addressed by Canales (1984), Gulunay (1986), Abma and Claerbout (1995), Soubaras (1995), and others. A more challenging problem of coherent noise attenuation has only recently joined the circle of the prediction technique applications (Spitz, 1999; Brown and Clapp, 2000; Guitton et al., 2001).

The problem has a very clear interpretation in terms of the local dip components. If two components, $\mathbf{s}_1$ and $\mathbf{s}_2$ are estimated from the data, and we can interpret the first component as signal, and the second component as noise, then the signal and noise separation problem reduces to solving the least-squares system

$$\mathbf{C}(\mathbf{s}_1)\mathbf{d}_1 \approx 0 , \tag{19}$$

$$\varepsilon \mathbf{C}(\mathbf{s}_2)\mathbf{d}_2 \approx 0 \tag{20}$$

for the unknown signal and noise components $\mathbf{d}_1$ and $\mathbf{d}_2$ of the input data $\mathbf{d}$:

$$\mathbf{d}_1 + \mathbf{d}_2 = \mathbf{d}. \tag{21}$$

The scalar parameter ε in equation (20) reflects the signal to noise ratio. We can combine equations (19-20) and (21) in the explicit system for the noise component $\mathbf{d}_2$:

$$\mathbf{C}(\mathbf{s}_1)\mathbf{d}_2 \approx \mathbf{C}(\mathbf{s}_1)\mathbf{d}, \tag{22}$$

$$\varepsilon \mathbf{C}(\mathbf{s}_2)\mathbf{d}_2 \approx 0. \tag{23}$$

Figure 16 shows a simple example of the described approach. I estimated two dip components from the input synthetic data and separated the corresponding events by solving the least-squares system (22-23). The separation result is visually perfect.

Figure 17 presents a significantly more complicated case: a receiver line from of a 3-D land shot gather from Saudi Arabia, contaminated with three-dimensional ground-roll, which appears hyperbolic in the cross-section. The same dataset has been used previously by Brown and Clapp (2000). The ground-roll noise and the reflection events have a significantly different frequency content, which might suggest separating them on the base of frequency alone. The result of frequency-based separation, shown in Figure 18 is, however, not ideal: part of the noise remains in the estimated signal after the separation. Changing the ε parameter in equation (23) could clean up the signal estimate, but it would also bring some of the signal into the subtracted noise. A better strategy is to separate the events by using both the difference in frequency and the difference in slope. For that purpose, I adopted the following algorithm:

1. Use a frequency-based separation (or, alternatively, a simple low-pass filtering) to obtain an initial estimate of the ground-roll noise.

2. Select a window around the initial noise. The further separation will happen only in that window.

3. Estimate the noise dip from the initial noise estimate.

4. Estimate the signal dip in the selected data window as the complimentary dip component to the already known noise dip.

5. Use the signal and noise dips together with the signal and noise frequencies to perform the final separation. This is achieved by cascading single-dip plane-wave destruction filters with local 1-D three-coefficient PEFs aimed at destroying a particular frequency.

The separation result is shown in Figure 19. The separation goal has been fully achieved: the estimated ground-roll noise is free of the signal components, and the estimated signal is free of the noise.

The left plot in Figure 20 shows another test example: a shot gather from Yilmaz and Cumro (1983), which is contaminated by nearly linear low-velocity noise. In this case, a simple dip-based separation was sufficient for achieving a good result. The algorithm proceeds as follows:

1. Bandpass the original data with an appropriate low-pass filter to obtain an initial noise estimate (the right plot in Figure 20.)

2. Estimate the local noise dip from the initial noise model.

3. Estimate the signal dip from the input data as the complimentary dip component to the already known noise dip.

4. Estimate the noise by an iterative optimization of system (22-23) and subtract it from the data to get the signal estimate.

Figure 21 shows the separation result. The signal and noise components are accurately separated.

The examples in this subsection show that when the signal and noise components have distinctly different local slopes, we can successfully separate them with plane-wave destruction filters.

CONCLUSIONS

Plane-wave destruction filters with an improved finite-difference design can be a valuable tool in processing multidimensional seismic data. On several examples, I showed their good performance in such problems as fault detection, missing data interpolation, and noise attenuation. Although only 2-D examples were demonstrated, it is straightforward to extend the method to 3-D applications by considering two orthogonal plane-wave slopes.

The similarities and differences between plane-wave destructors and T-X prediction-error filters can be summarized as follows:

Similarities:

- Both types of filters operate in the original time-and-space domain of recorded data.
- Both filters aim to predict local plane-wave events in the data.
- In most problems, one filter type can be replaced by the other, and certain techniques, such as Claerbout's trace interpolation method, are common for both approaches.

Differences:

- The design of plane-wave destructors is purely deterministic and follows the plane-wave differential equation. The design of T-X PEF has statistical roots in the framework of the

maximum-entropy spectral analysis (Burg, 1975). In principle, T-X PEF can characterize more complex signals than local plane waves.

- In the case of PEF, we estimate filter coefficients. In the case of plane-wave destructors, the estimated quantity is the local plane-wave slope. Several important distinctions follow from that difference:
  - The filter-estimation problem is linear. The slope estimation problem, in the case of the improved filter design, is non-linear, but allows for an iterative linearization. In general, non-linearity is an undesirable feature because of local minima and the dependence on initial conditions. However, we can sometimes use it creatively. For example, it helped to avoid aliased dips in the trace interpolation example.
  - Non-stationarity is handled gracefully in the local slope estimation. No local windows are required to produce a smoothly varying estimate of the local slope. This is a much more difficult issue for PEFs because of the largely under-determined problem.
  - Local slope has a clearly interpretable physical meaning, which allows for easy quality control of the results. The coefficients of T-X PEFs are much more difficult to interpret.
- The efficiency of the two approaches is difficult to compare. Plane-wave destructors are generally more efficient to apply because of the small number of filter coefficients. However, they may require more computation at the estimation stage because of the non-linearity problem.

ACKNOWLEDGMENTS

This work was partially accomplished at the Stanford Exploration Project (SEP).

I would like to thank Jon Claerbout, Robert Clapp, Matthias Schwab, and other SEP members

for developing and maintaining the reproducible research technology, which helped this research.

Suggestions from two anonymous reviewers helped to improve the paper.

REFERENCES

Abma, R., and Claerbout, J., 1995, Lateral prediction for noise attenuation by t-x and F-X techniques: Geophysics, **60**, no. 06, 1887–1896.

Bednar, J. B., 1998, Least squares dip and coherency attributes: 68th Ann. Internat. Mtg, Soc. Expl. Geophys., Expanded Abstracts, 653–655.

Brown, M., and Clapp, R., 2000, T-X domain, pattern-based ground-roll removal: 70th Annual Internat. Mtg., Soc. Expl. Geophys., Expanded Abstracts, 2103–2106.

Burg, J. P., 1975, Maximum entropy spectral analysis: Ph.D. thesis, Stanford University.

Canales, L. L., 1984, Random noise reduction: 54th Annual Internat. Mtg., Soc. Expl. Geophys., Expanded Abstracts, Session:S10.1.

Claerbout, J., and Brown, M., 1999, Two-dimensional textures and prediction-error filters: 61st Mtg. Eur. Assoc. Expl. Geophys., Eur. Assoc. Expl. Geophys., Abstracts, Session:1009.

Claerbout, J. F., 1992, Earth Soundings Analysis: Processing Versus Inversion: Blackwell Scientific Publications.

Claerbout, J. F., 1994, Applications of two- and three-dimensional filtering: 64th Ann. Internat. Mtg, Soc. Expl. Geophys., Expanded Abstracts, 1572–1575.

Claerbout, J., 1998, Multidimensional recursive filters via a helix: Geophysics, **63**, no. 05, 1532–1541.

Claerbout, J., 1999, Geophysical estimation by example: Environmental soundings image enhancement: Stanford Exploration Project, http://sepwww.stanford.edu/sep/prof/.

Clapp, R., Biondi, B., Fomel, S., and Claerbout, J., 1998, Regularizing velocity estimation using geologic dip information: 68th Ann. Internat. Meeting, Soc. Expl. Geophys., Expanded Abstracts, 1851–1854.

Clapp, R. G., 2000, Geologically constrained migration velocity analysis: Ph.D. thesis, Stanford University.

Crawley, S., Clapp, R., and Claerbout, J., 1999, Interpolation with smoothly nonstationary prediction-error filters: 69th Ann. Internat. Meeting, Soc. Expl. Geophys., Expanded Abstracts, 1154–1157.

Crawley, S., 2000, Seismic trace interpolation with nonstationary prediction-error filters: Ph.D. thesis, Stanford University.

Fomel, S., and Claerbout, J. F., 2001, Multidimensional recursive filter preconditioning in geophysical estimation problems: submitted to Geophysics.

Fomel, S., 2000, Three-dimensional seismic data regularization: Ph.D. thesis, Stanford University.

Freeman, W. T., and Adelson, E. H., 1991, The design and use of steerable filters: IEEE Trans. on Pattern Analysis and Machine Intelligence, **1**, no. 9, 891–906.

Guitton, A., Brown, M., Rickett, J., and Clapp, R., 2001, Multiple attenuation using a t-x pattern-based subtraction method: 71st Ann. Internat. Mtg, Soc. Expl. Geophys., Expanded Abstracts, 1305–1308.

Gulunay, N., 1986, Fx decon and complex Wiener prediction filter: 56th Ann. Internat. Mtg., Soc. Expl. Geophys., Expanded Abstracts, Session:POS2.10.

Harlan, W. S., Claerbout, J. F., and Rocca, F., 1984, Signal/noise separation and velocity estimation: Geophysics, **49**, no. 11, 1869–1880.

Kim, S., and Symes, W. W., 1998, Smooth detectors of linear phase: Inverse Problems, **14**, 101–112.

Neidell, N. S., and Taner, M. T., 1971, Semblance and other coherency measures for multichannel data: Geophysics, **36**, no. 03, 482–497.

Nichols, D., 1990, Estimation of missing data by least squares: SEP–**65**, 271–294.

Schwab, M., Claerbout, J., and Holden, C., 1996, Revealing geological discontinuities by plane reflector suppression: 66th Annual Internat. Mtg., Soc. Expl. Geophys., Expanded Abstracts, 302–305.

Schwab, M., 1998, Enhancement of discontinuities in seismic 3-D images using a Java estimation library: Ph.D. thesis, Stanford University.

Simoncelli, E. P., and Farid, H., 1996, Steerable wedge filters for local orientation analysis: IEEE Trans. on Image Processing, **5**, no. 9, 1377–1382.

Soubaras, R., 1995, Prestack random and impulsive noise attenuation by F-X projection filtering: 65th Ann. Internat. Mtg, Soc. Expl. Geophys., Expanded Abstracts, 711–714.

Spitz, S., 1991, Seismic trace interpolation in the f-x domain: Geophysics, **56**, no. 6, 785–794.

Spitz, S., 1999, Pattern recognition, spatial predictability, and subtraction of multiple events: The Leading Edge, **18**, no. 1, 55–58.

Symes, W. W., and Carazzone, J. J., 1991, Velocity inversion by differential semblance optimization: Geophysics, **56**, no. 05, 654–663.

Symes, W. W., 1994, The plane wave detection problem: Inverse Problems, **10**, 1361–1391.

Yilmaz, O., and Cumro, D., 1983, Worldwide assortment of field seismic records, released by Western Geophysical Company of America: Houston.

APPENDIX A

DETERMINING FILTER COEFFICIENTS BY TAYLOR EXPANSION

This appendix details the derivation of equations (9) and (10). The main idea to match the frequency responses of the approximate plane-wave filters to the response of the exact phase-shift operator at low frequencies.

The Taylor series expansion of the phase-shift operator $e^{i\omega\sigma}$ around the zero frequency $\omega = 0$ takes the form

$$e^{i\omega\sigma} \approx 1 + i\,\sigma\omega - \frac{\sigma^2\,\omega^2}{2} - i\,\frac{\sigma^3\,\omega^3}{6} + O\left(\omega^4\right) \tag{A-1}$$

The Taylor expansion of the six-point implicit finite-difference operator takes the form

$$\begin{aligned}
\frac{B_3(Z_t)}{B_3(1/Z_t)} &= \frac{b_{-1}Z_t^{-1} + b_0 + b_1 Z_t}{b_1 Z_t + b_0 + b_{-1}Z_t^{-1}} = \frac{b_{-1}\,e^{-i\omega} + b_0 + b_1\,e^{i\omega}}{b_1\,e^{-i\omega} + b_0 + b_{-1}\,e^{i\omega}} \\
&\approx 1 - \frac{2\,i\,(b_{-1} - b_1)\,\omega}{b_0 + b_{-1} + b_1} - \frac{2\,(b_{-1} - b_1)^2\,\omega^2}{(b_0 + b_{-1} + b_1)^2} \\
&\quad + \frac{i\,(b_{-1} - b_1)\left[b_0^2 - b_0\,(b_{-1} + b_1)4\,\left(b_{-1}^2 - 4b_{-1}\,b_1 + b_1{}^2\right)\right]\omega^3}{3\,(b_0 + b_{-1} + b_1)^3} + \ldots
\end{aligned} \tag{A-2}$$

Matching the corresponding terms of expansions (A-1) and (A-2), we arrive at the system of non-linear equations

$$\sigma = \frac{2\,(b_1 - b_{-1})}{b_0 + b_{-1} + b_1} \tag{A-3}$$

$$\sigma^2 = \frac{4\,(b_1 - b_{-1})^2}{(b_0 + b_{-1} + b_1)^2} \tag{A-4}$$

$$\sigma^3 = \frac{2\,(b_1 - b_{-1})\left[b_0^2 - b_0\,(b_{-1} + b_1) + 4\,\left(b_{-1}^2 - 4b_{-1}\,b_1 + b_1^2\right)\right]}{(b_0 + b_{-1} + b_1)^3} \tag{A-5}$$

System (A-3-A-5) does not uniquely constrain the filter coefficients b_{-1}, b_0, and b_1 because equation (A-4) simply follows from (A-3) and because all the coefficients can be multiplied simultaneously by an arbitrary constant without affecting the ratios in equation (A-2). I chose an additional

constraint in the form

$$B_3(1) = b_{-1} + b_0 + b_1 = 1\,, \tag{A-6}$$

which ensures that the filter $B_3(Z_t)$ does not alter the zero frequency component. System (A-3-A-5) with the additional constraint (A-6) resolves uniquely to the coefficients of filter (9) in the main text:

$$b_{-1} = \frac{(1-\sigma)(2-\sigma)}{12}\,; \tag{A-7}$$

$$b_0 = \frac{(2+\sigma)(2-\sigma)}{6}\,; \tag{A-8}$$

$$b_1 = \frac{(1+\sigma)(2+\sigma)}{12}\,. \tag{A-9}$$

The B_5 filter of equation (10) is constructed in a completely analogous way, using longer Taylor expansions to constrain the additional coefficients. Generalization to longer filters is straightforward.

The technique of this appendix aims at matching the filter responses at low frequencies. One might construct different filter families by employing other criteria for filter design (least squares fit, equiripple, etc.)

LIST OF FIGURES

1 Phase of the implicit finite-difference shift operators in comparison with the exact solution. The left plot corresponds to the slope of $\sigma = 0.5$, the right plot to $\sigma = 0.8$.

2 Synthetic sedimentary model. Left plot: Input data. Right plot: Its texture. The texture is computed by convolving a field number with the inverse of plane-wave destruction filters. It highlights the position of estimated local plane waves.

3 Synthetic sedimentary model. Left plot: Estimated dip field. Right plot: Prediction residual. Large absolute residual indicates the location of faults.

4 Prediction residual of the 11-point prediction-error filter estimated in local 20x6 windows (reproduced from (Claerbout, 1999)).To be compared with the right plot in Figure 3.

5 Conflicting dips synthetic. Left plot: Input data. Right plot: Its texture.

6 Conflicting dips synthetic. Left plot: Estimated dip field. Right plot: Prediction residual.Large absolute residual indicates the location of conflicting dips.

7 Real shot gather. Left plot: Input data. Right plot: Its texture.

8 Real shot gather. Left plot: Estimated dip field. Right plot: Prediction residual. The residual highlights surface waves hidden under dominant reflection events in the original data.

9 Time section from the Gulf of Mexico. Left plot: Input data. Right plot: Its texture. The texture plot shows dominant local dips estimated from the data.

10 Time section from the Gulf of Mexico. Left plot: Estimated dip field. Right plot: Prediction residual.The residual highlights diffraction events hidden under dominant reflections in the original data.

11 Synthetic example of interpolation beyond aliasing with plane-wave destruction filters. Left: input aliased data, right: interpolation output.Three additional traces were inserted between

each of the neighboring input traces.

12 2-D marine shot gather. Left: original. Right: subsampled by a factor of two in the offset direction.

13 Two components of the estimated dip field for the decimated 2-D marine shot gather.

14 Left: 2-D marine shot gather after trace interpolation. Right: Difference between the interpolated and the original gather. The error is zero at the location of original traces and fairly random at the location of inserted traces.

15 Close-up comparison of the interpolated (right) and the original data (left).

16 Simple example of dip-based single and noise separation. From left to right: ideal signal, input data, estimated signal, estimated noise.

17 Ground-roll-contaminated data from Saudi Arabian sand dunes. A reciever cable out of a 3-D shot gather.

18 Signal and noise separation based on frequency. Top: estimated signal. Bottom: estimated noise.

19 Signal and noise separation based on both apparent dip and frequency in the considered receiver cable. Top: estimated signal. Bottom: estimated noise.

20 Left: Input noise-contaminated shot gather. Right: Result of low-pass filtering. The filtered data is is used as a noise model to estimate the noise dip.

21 Signal and noise separation based on dip. Left: estimated signal. Right: estimated noise.

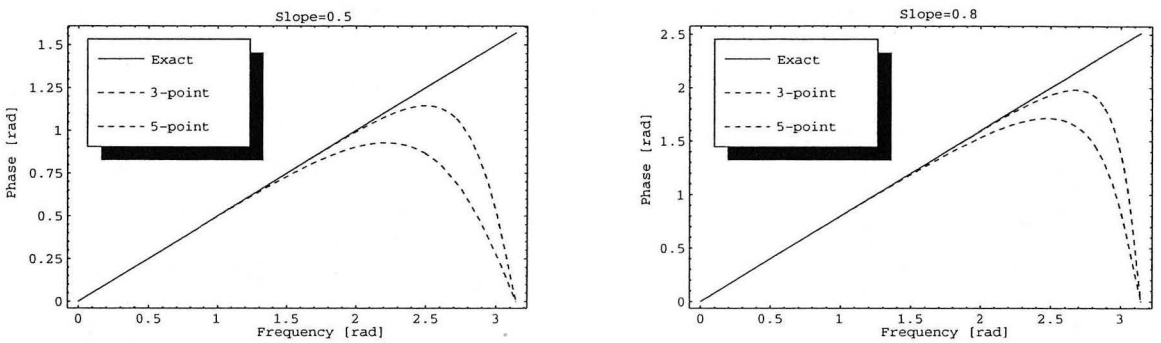
Slope=0.5
Exact
3-point
5-point
Phase [rad]
Frequency [rad]
Slope=0.8
Exact
3-point
5-point
Phase [rad]
Frequency [rad]

Figure 1.

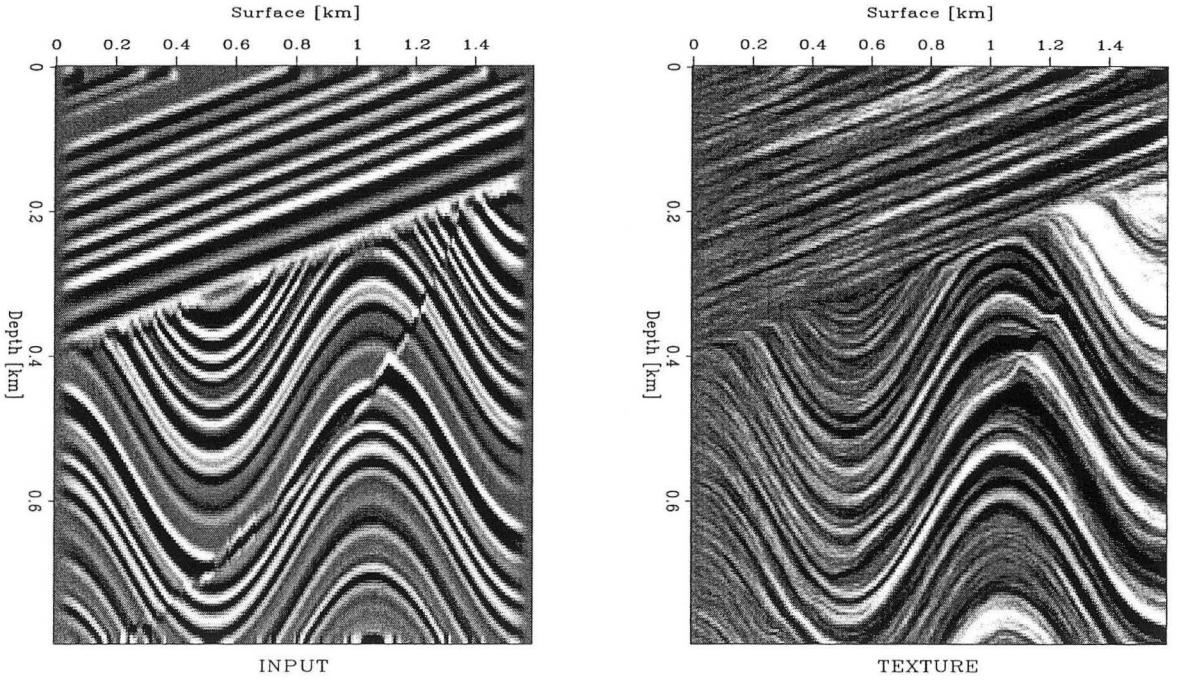
Surface [km]
0
0.2
0.4
0.6
0.8
1
1.2
1.4
Depth [km]
0
0.2
0.4
0.6
INPUT
Surface [km]
0
0.2
0.4
0.6
0.8
1
1.2
1.4
Depth [km]
0
0.2
0.4
0.6
TEXTURE

Figure 2.

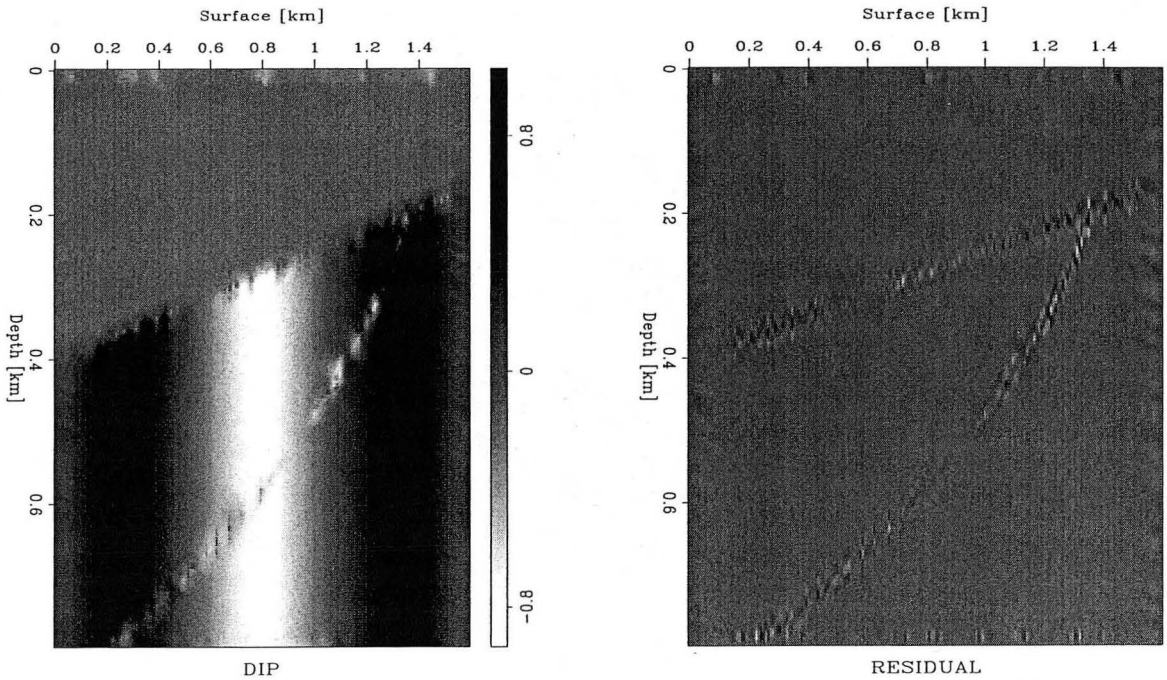
Surface [km]
0
0.2
0.4
0.6
0.8
1
1.2
1.4
Depth [km]
0
0.2
0.4
0.6
0.8
0
-0.8
DIP
Surface [km]
0
0.2
0.4
0.6
0.8
1
1.2
1.4
Depth [km]
0
0.2
0.4
0.6
RESIDUAL

Figure 3.

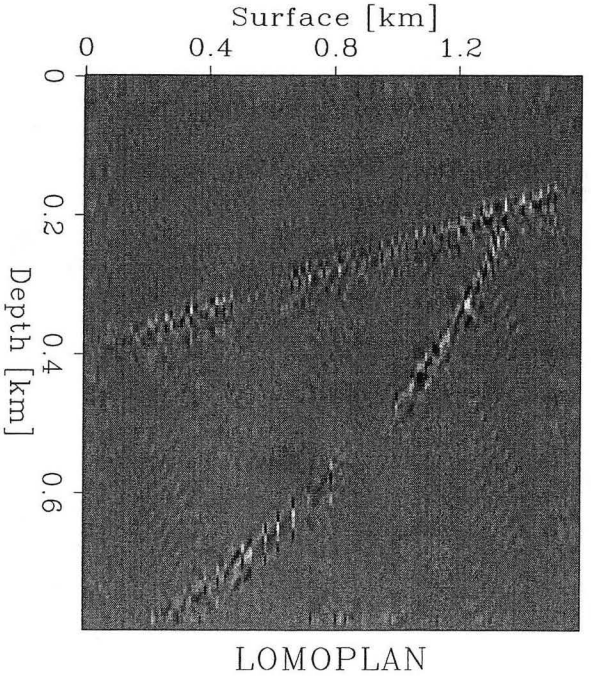

Figure 4.

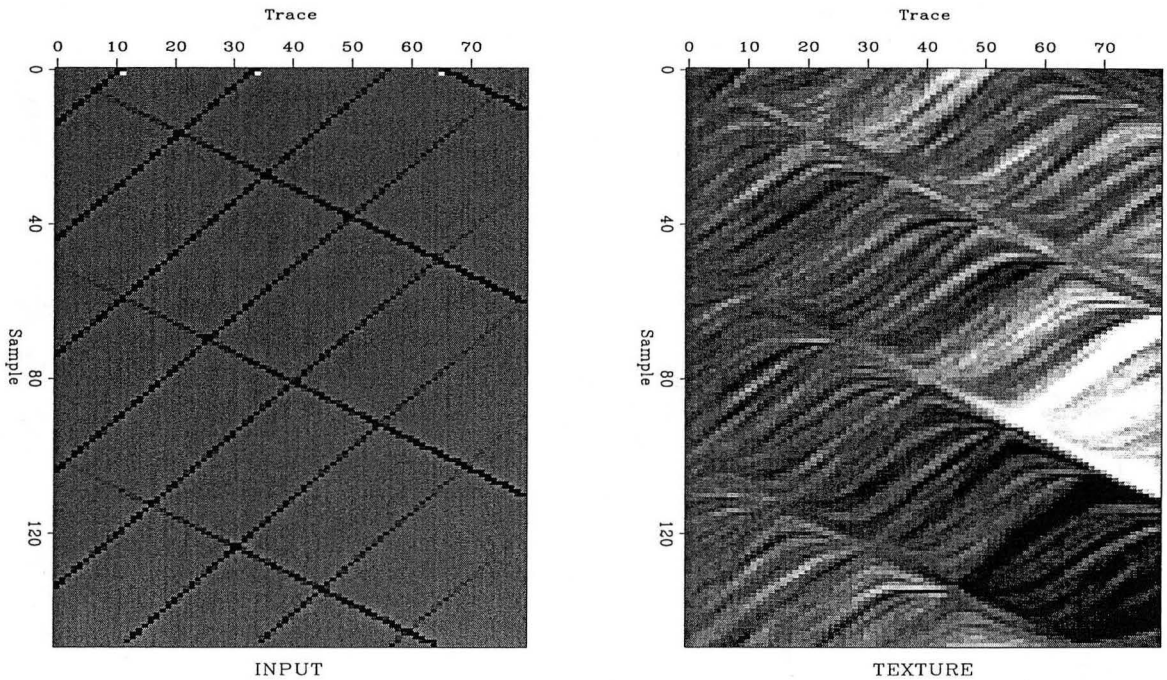
Trace
0
10
20
30
40
50
60
70
Sample
0
40
80
120
INPUT
Trace
0
10
20
30
40
50
60
70
Sample
0
40
80
120
TEXTURE

Figure 5.

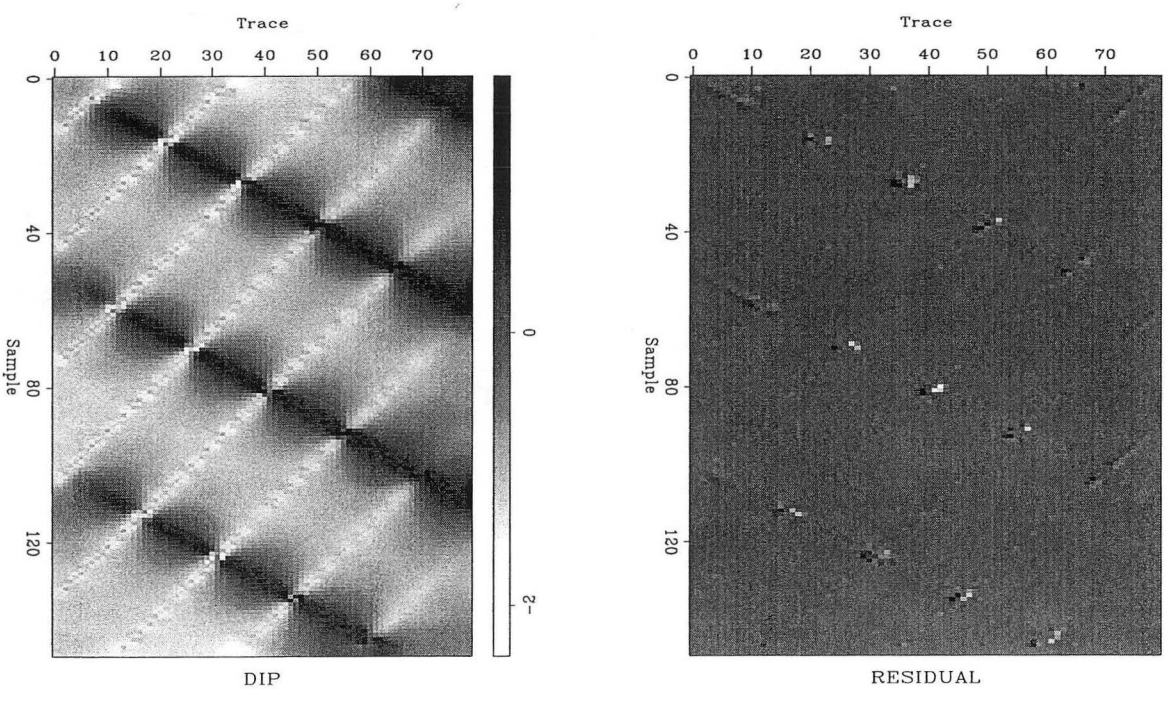
Trace
0 10 20 30 40 50 60 70
Sample
0 40 80 120
0
-2
DIP
Trace
0 10 20 30 40 50 60 70
Sample
0 40 80 120
RESIDUAL

Figure 6.

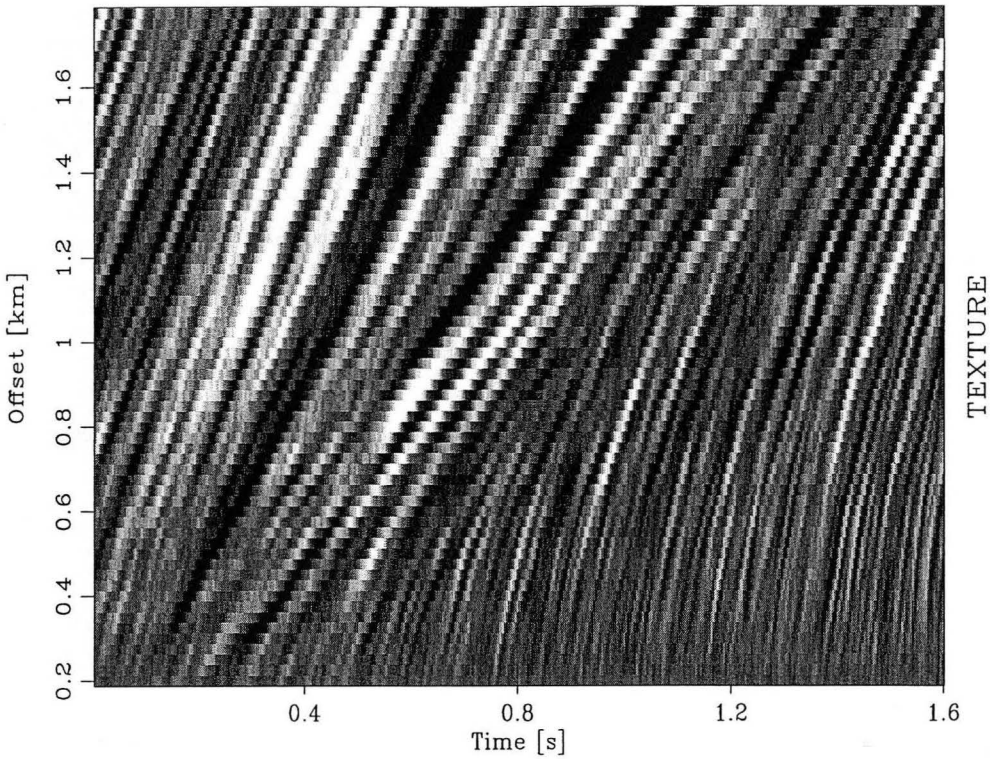
Offset [km]
0.2
0.4
0.6
0.8
1
1.2
1.4
1.6
0.4
0.8
1.2
1.6
Time [s]
TEXTURE

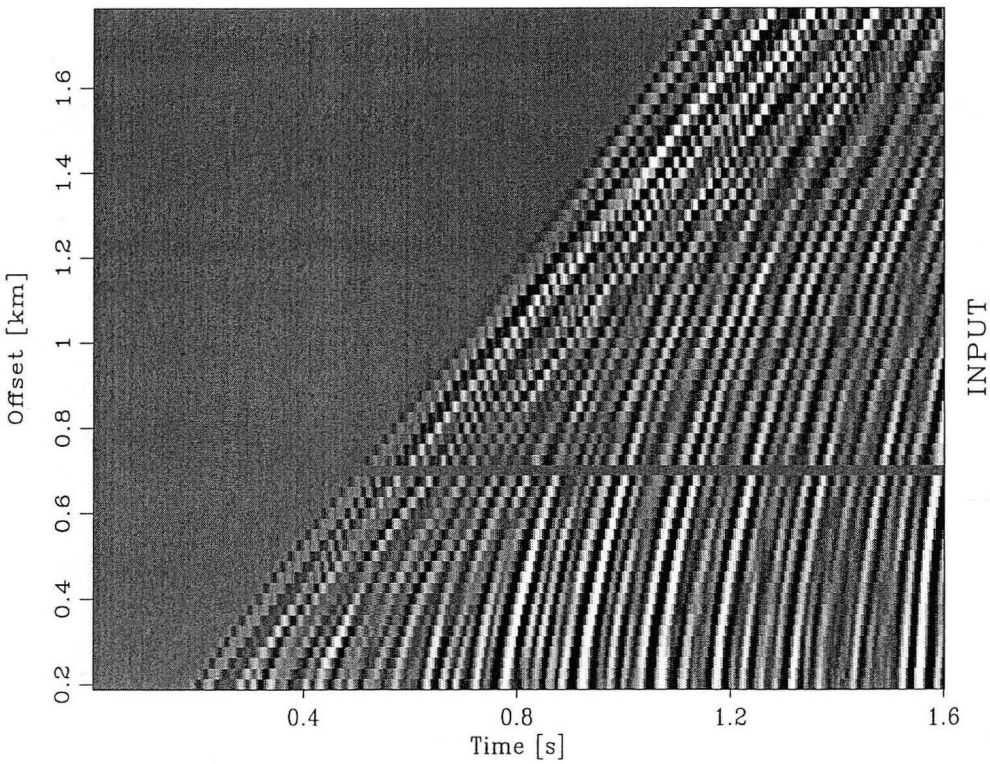
Offset [km]
0.2
0.4
0.6
0.8
1
1.2
1.4
1.6
0.4
0.8
1.2
1.6
Time [s]
INPUT

Figure 7.

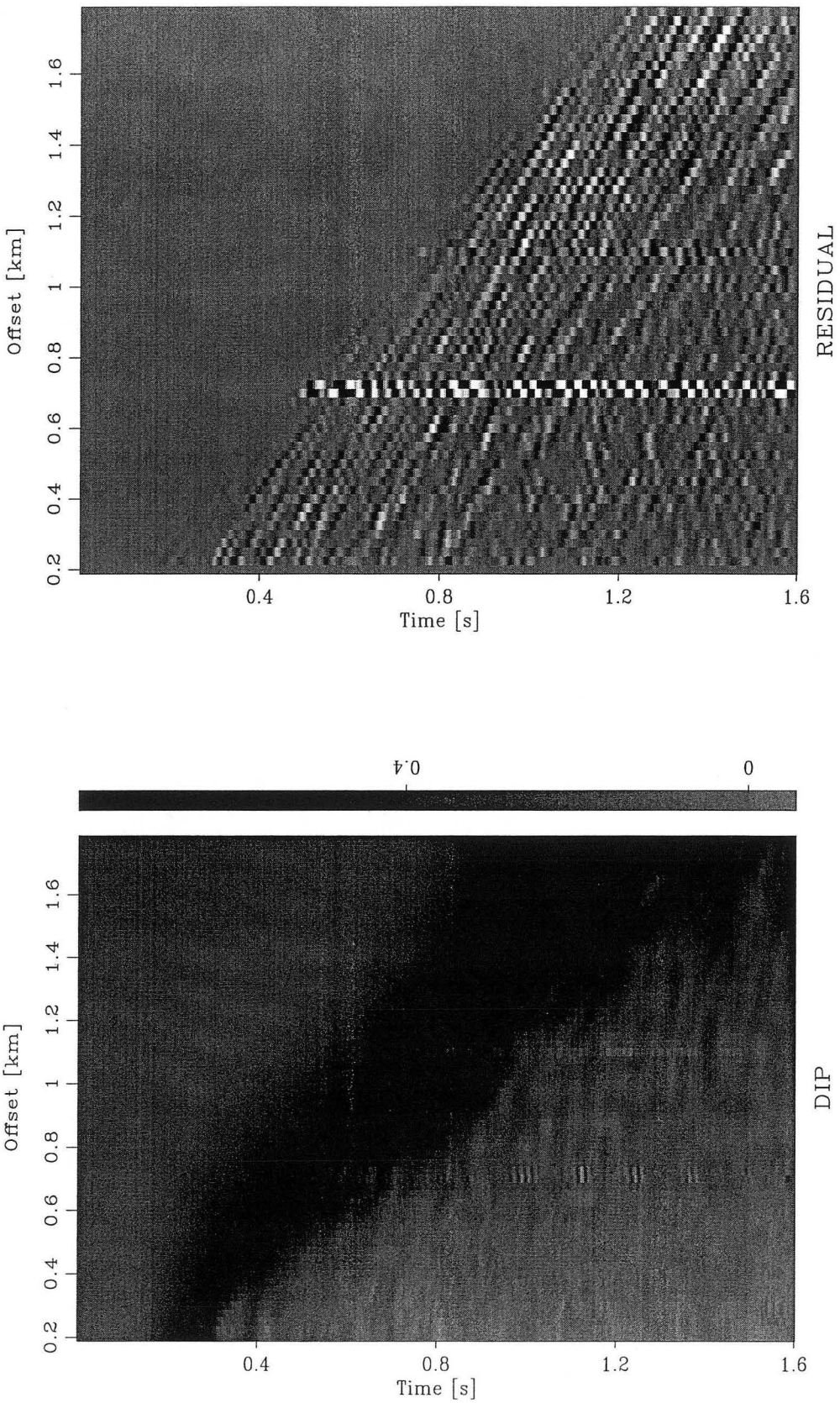
RESIDUAL
Offset [km]
0.2
0.4
0.6
0.8
1
1.2
1.4
1.6
Time [s]
0.4
0.8
1.2
1.6
DIP
Offset [km]
0.2
0.4
0.6
0.8
1
1.2
1.4
1.6
Time [s]
0.4
0.8
1.2
1.6
0
0.4

Figure 8.

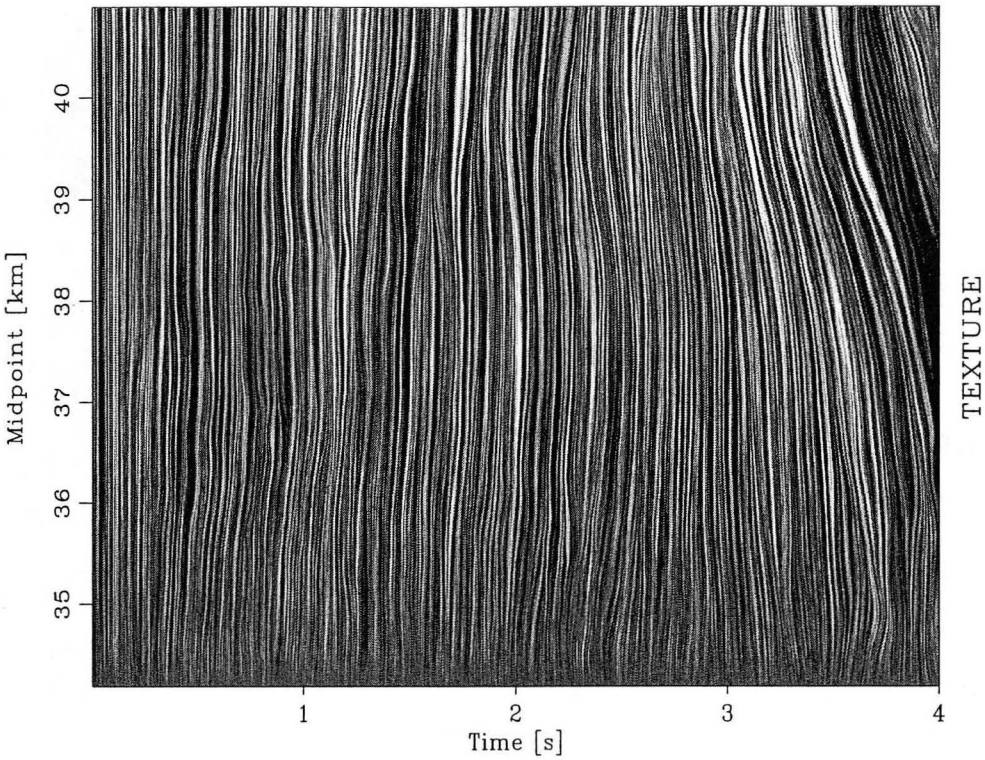
Midpoint [km]
35
36
37
38
39
40
1
2
3
4
Time [s]
TEXTURE

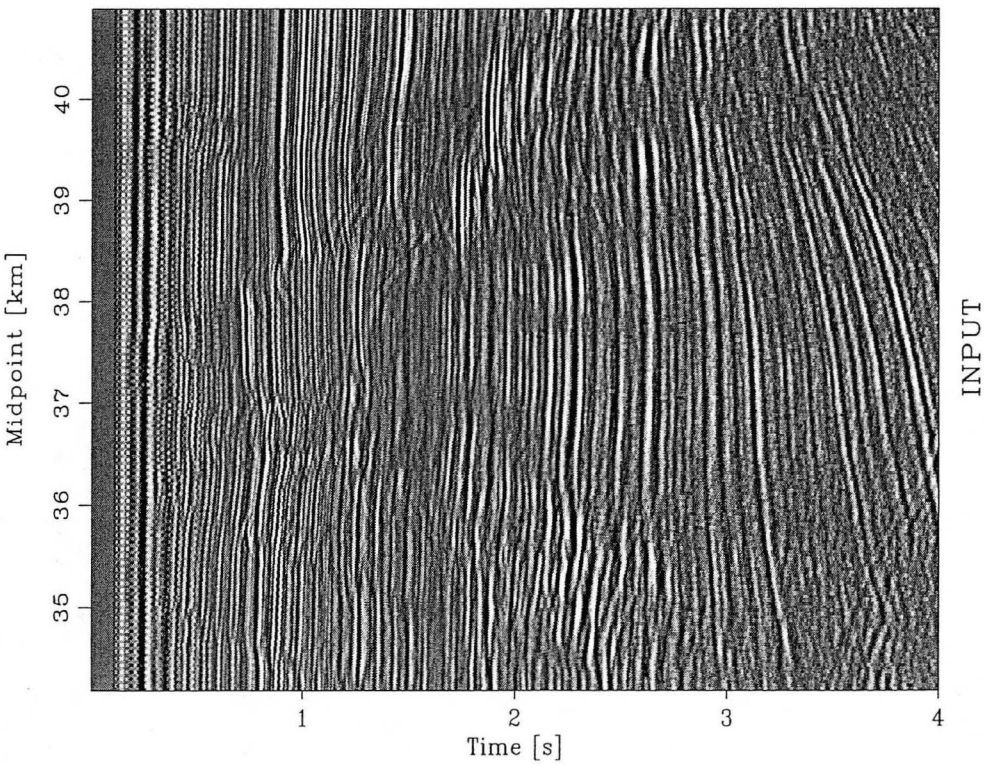
Midpoint [km]
35
36
37
38
39
40
1
2
3
4
Time [s]
INPUT

Figure 9.

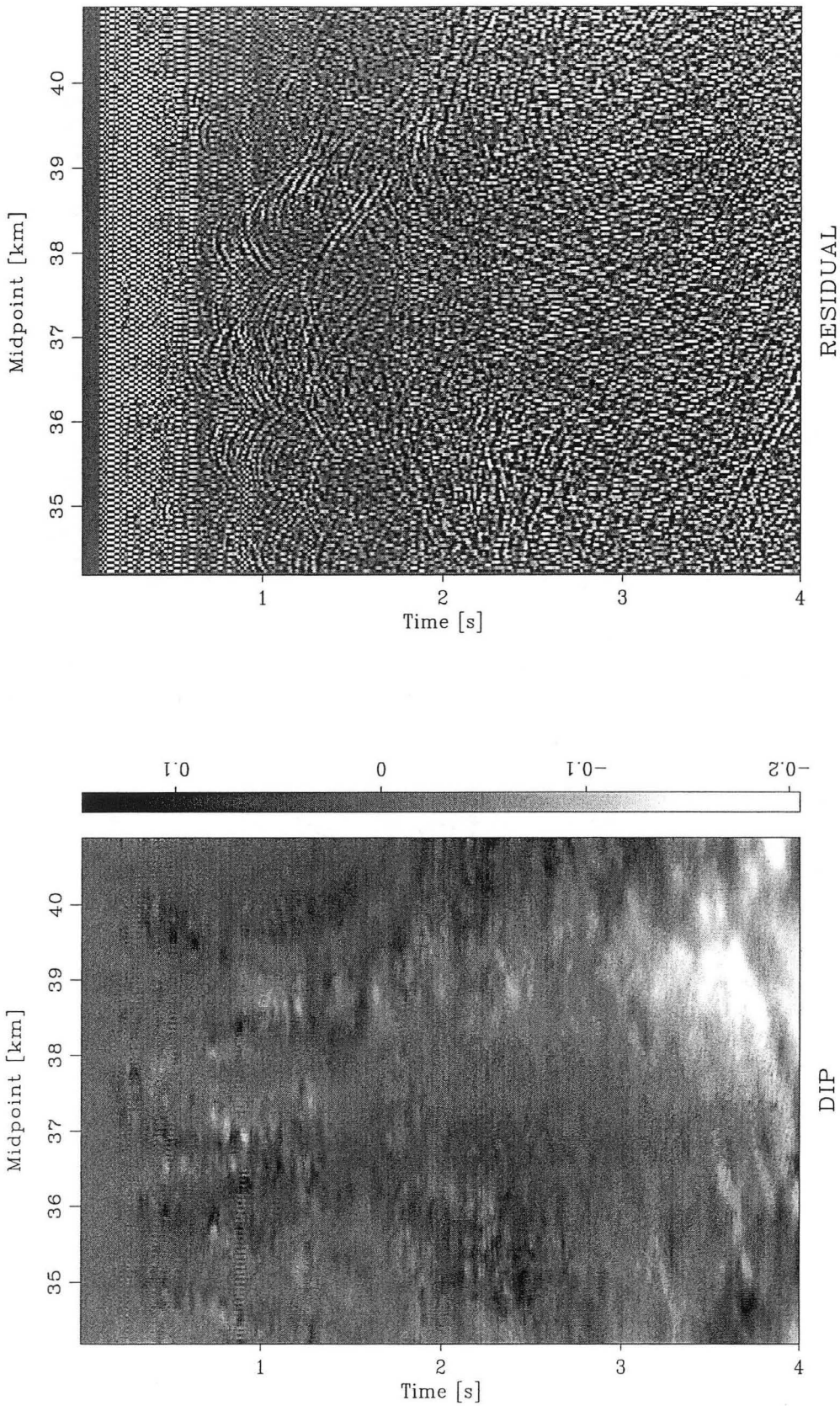
RESIDUAL
Midpoint [km]
35
36
37
38
39
40
Time [s]
1
2
3
4
DIP
Midpoint [km]
35
36
37
38
39
40
Time [s]
1
2
3
4
0.1
0
−0.1
−0.2

Figure 10.

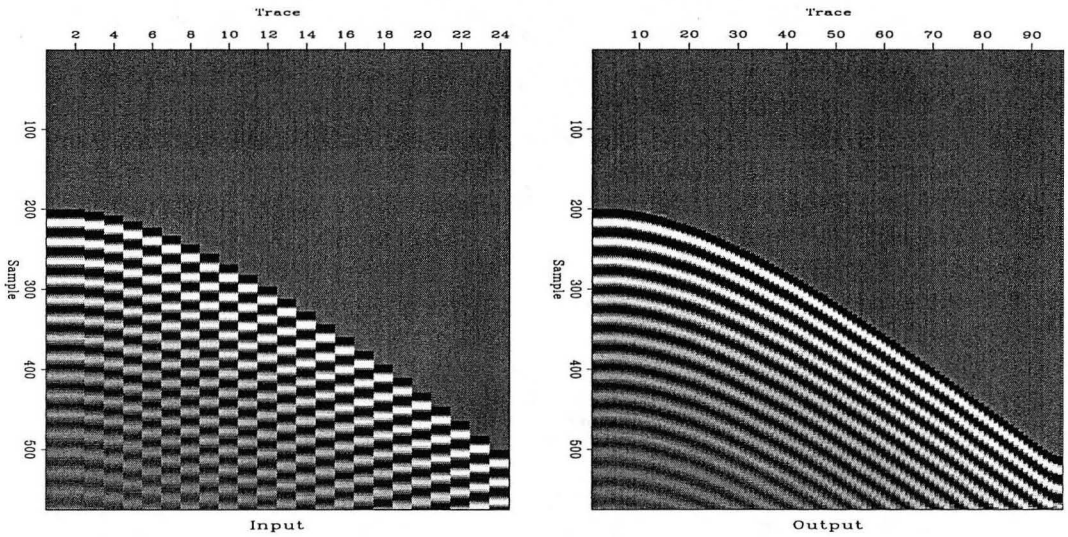
Trace
2 4 6 8 10 12 14 16 18 20 22 24
Sample
100 200 300 400 500
Input
Trace
10 20 30 40 50 60 70 80 90
Sample
100 200 300 400 500
Output

Figure 11.

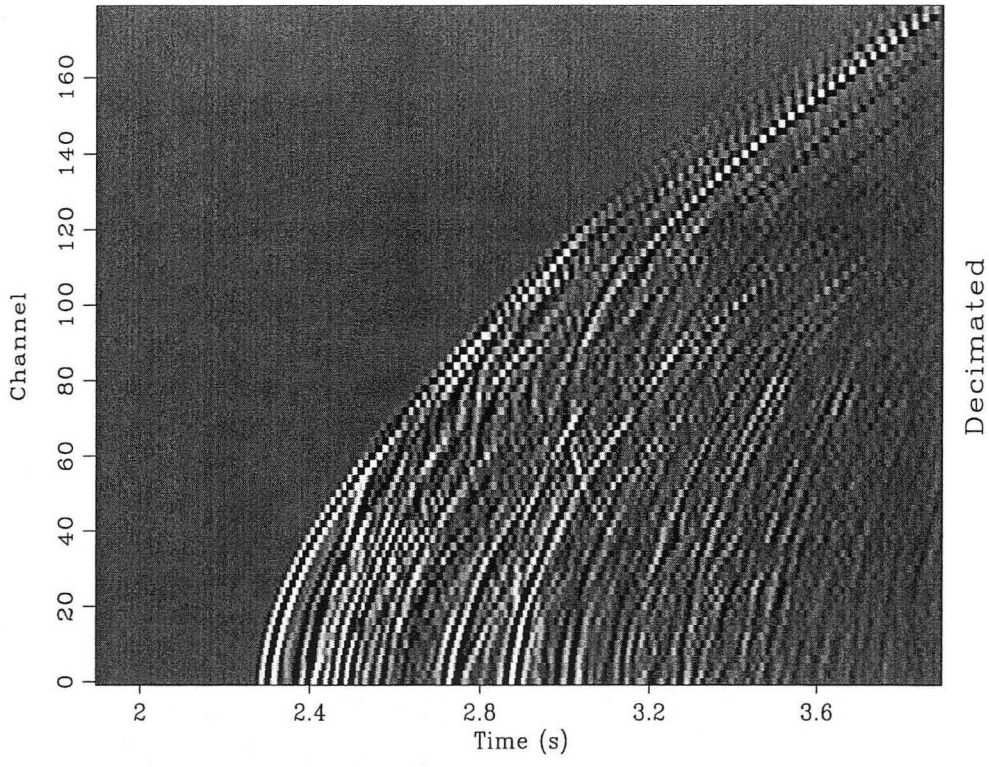
Channel
0
20
40
60
80
100
120
140
160
2
2.4
2.8
3.2
3.6
Time (s)
Decimated

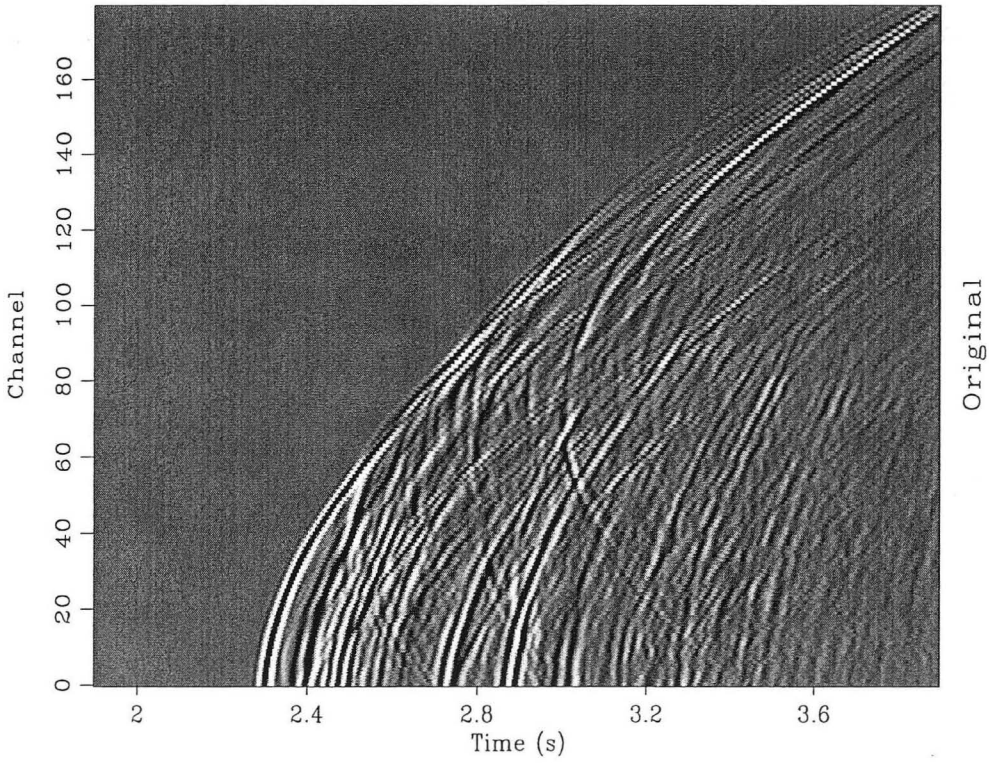
Channel
0
20
40
60
80
100
120
140
160
2
2.4
2.8
3.2
3.6
Time (s)
Original

Figure 12.

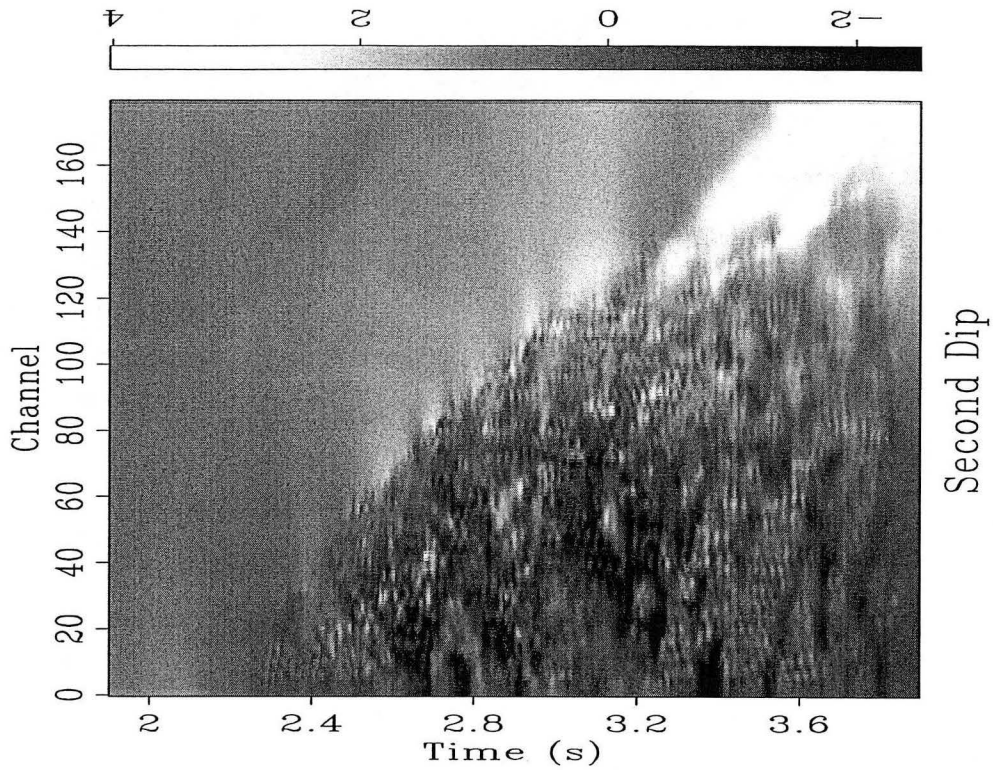
Second Dip
Channel
0
20
40
60
80
100
120
140
160
2
2.4
2.8
3.2
3.6
Time (s)
-2
0
2
4

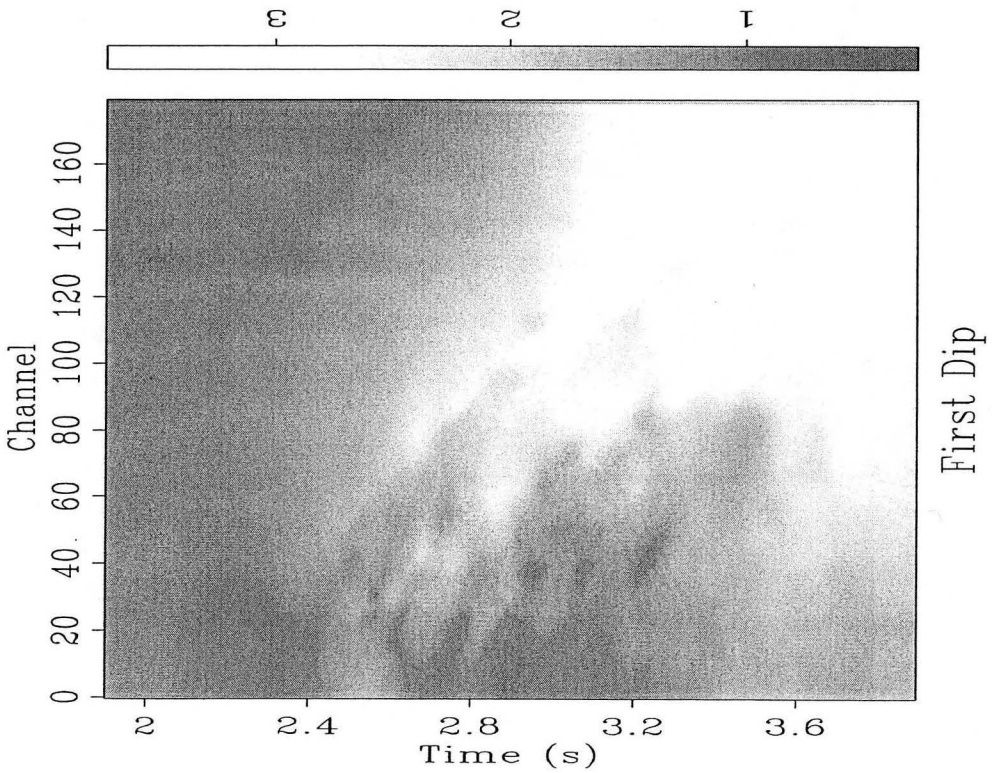
First Dip
Channel
0
20
40
60
80
100
120
140
160
2
2.4
2.8
3.2
3.6
Time (s)
1
2
3

Figure 13.

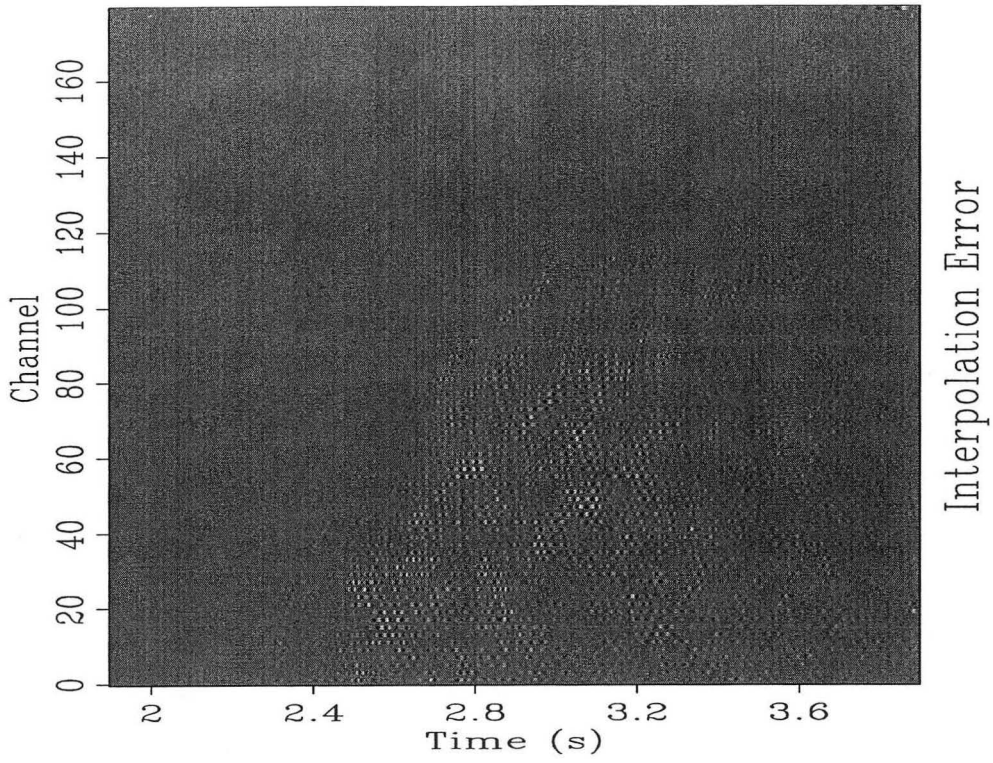
Interpolation Error
Channel
0
20
40
60
80
100
120
140
160
2
2.4
2.8
3.2
3.6
Time (s)

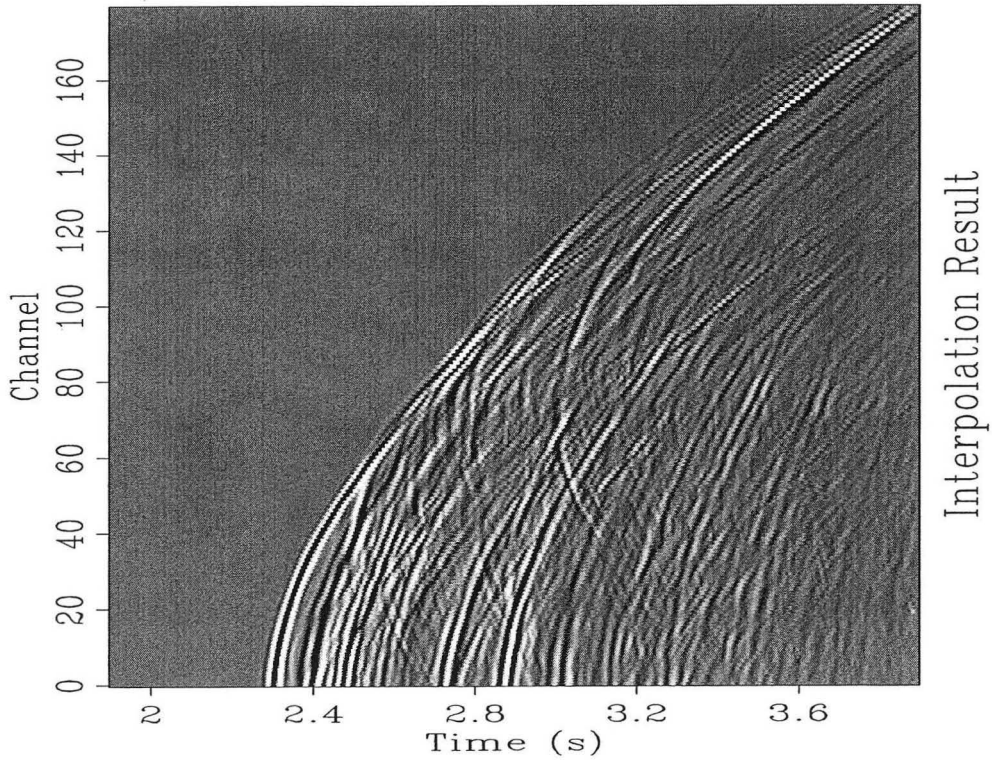
Interpolation Result
Channel
0
20
40
60
80
100
120
140
160
2
2.4
2.8
3.2
3.6
Time (s)

Figure 14.

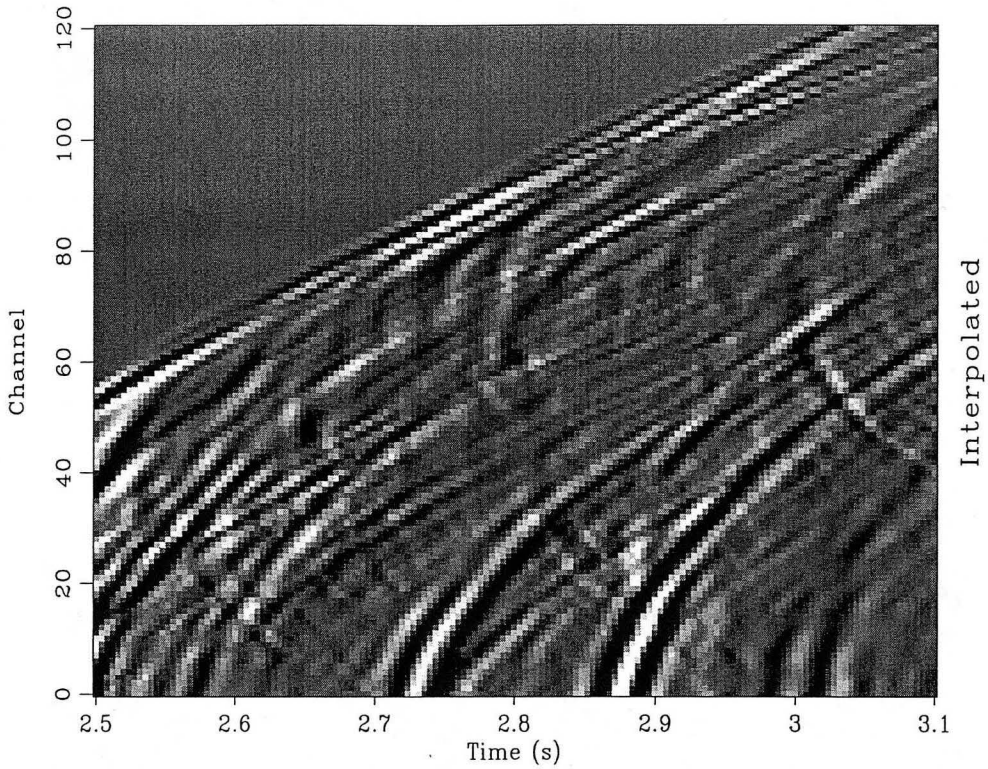
Channel
0
20
40
60
80
100
120
2.5
2.6
2.7
2.8
2.9
3
3.1
Time (s)
Interpolated

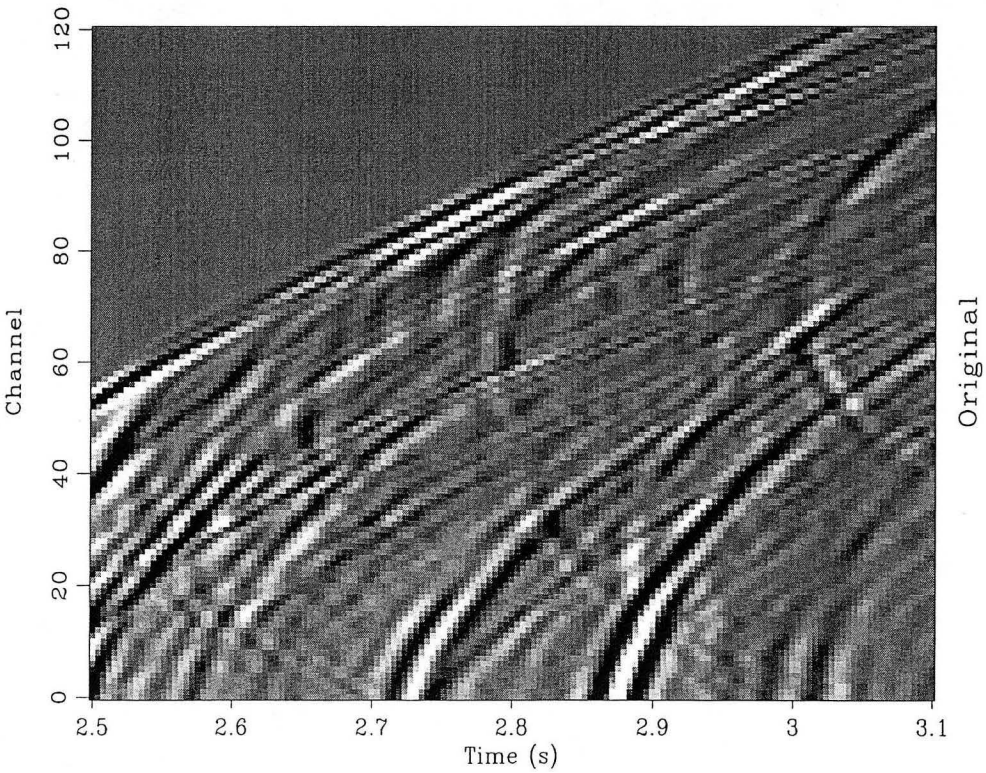
Channel
0
20
40
60
80
100
120
2.5
2.6
2.7
2.8
2.9
3
3.1
Time (s)
Original

Figure 15.

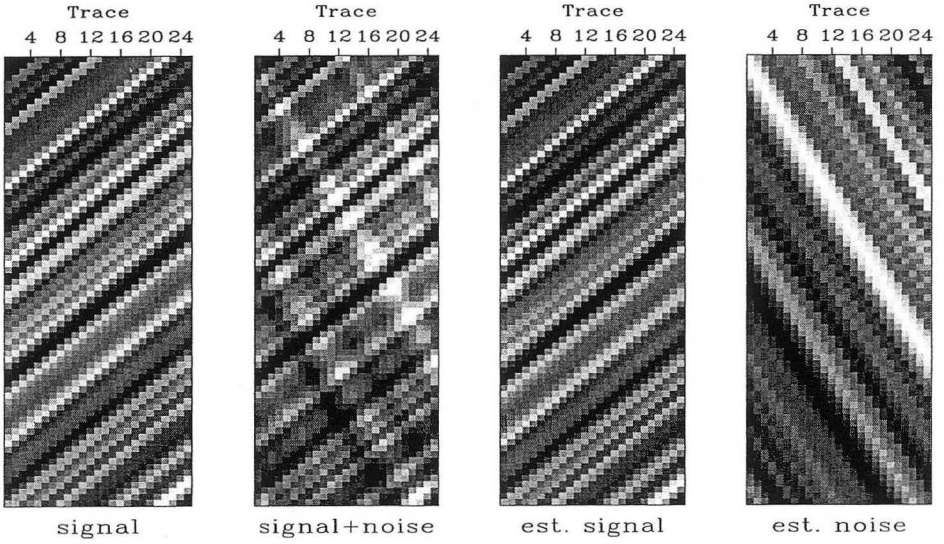
Trace
4 8 12 16 20 24
signal
Trace
4 8 12 16 20 24
signal+noise
Trace
4 8 12 16 20 24
est. signal
Trace
4 8 12 16 20 24
est. noise

Figure 16.

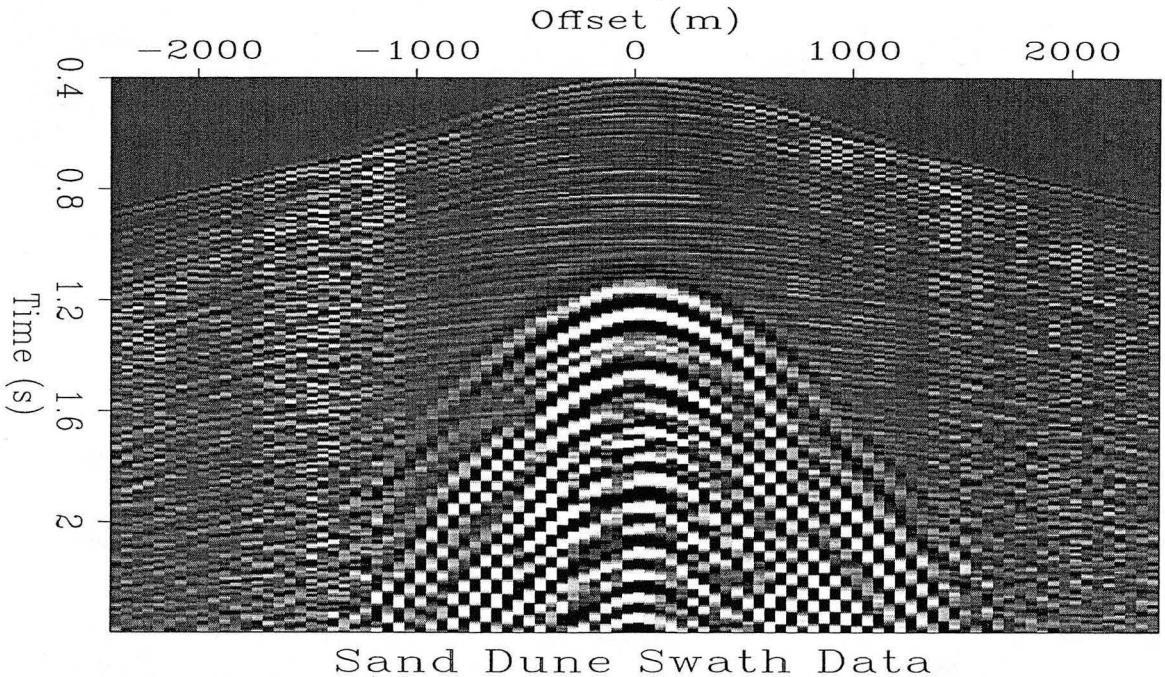
Offset (m)
−2000
−1000
0
1000
2000
0.4
0.8
1.2
1.6
2
Time (s)
Sand Dune Swath Data

Figure 17.

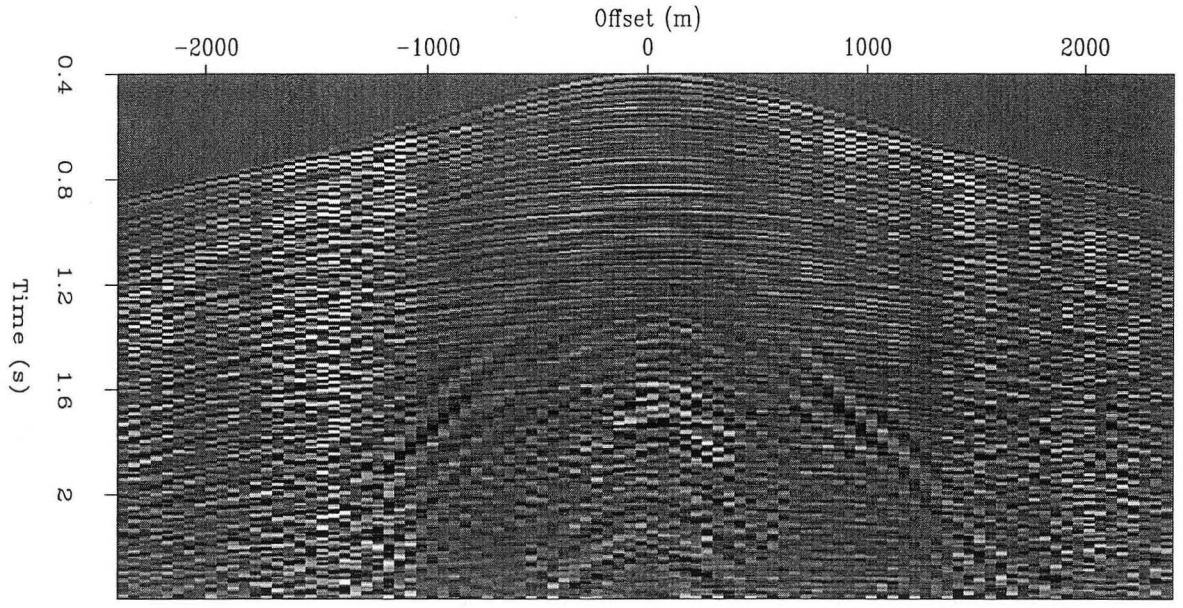

Estimated Signal

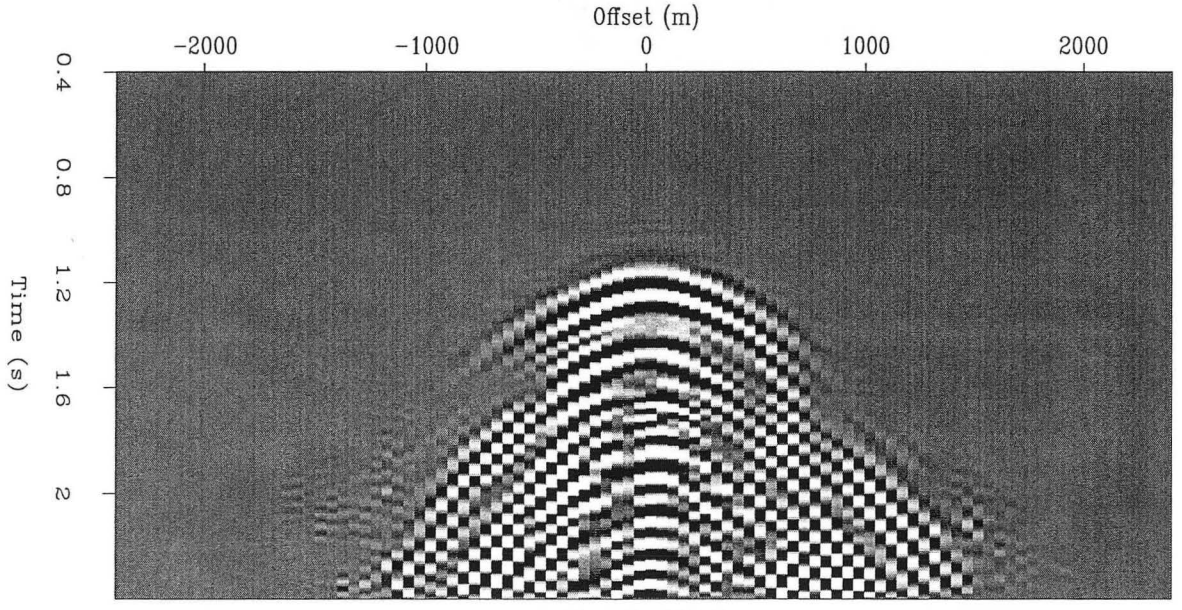

Estimated Noise

Figure 18.

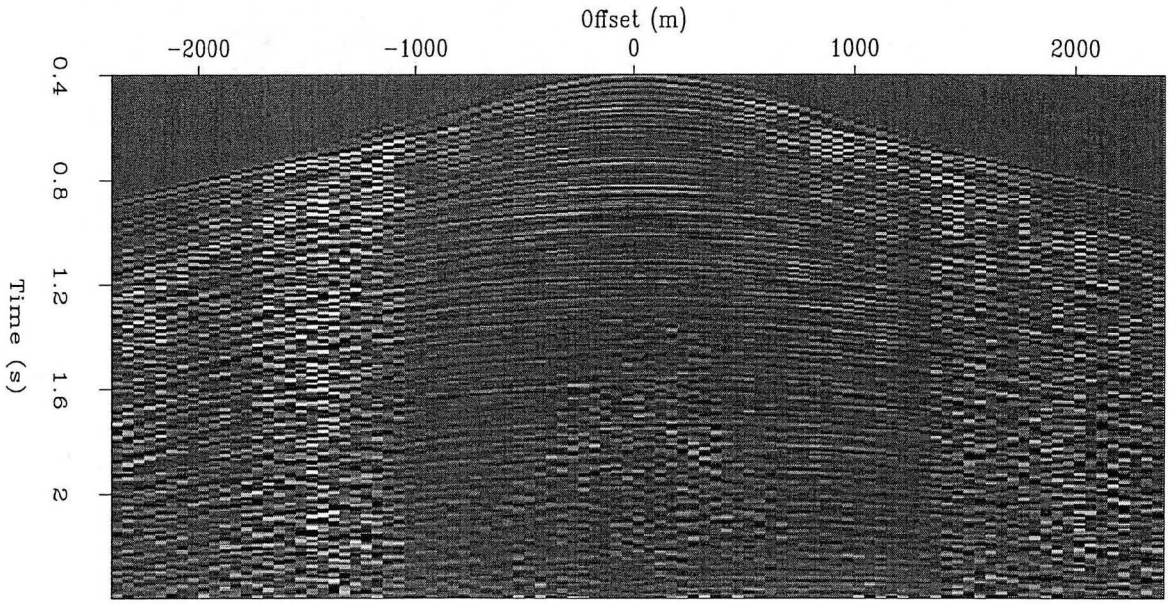

Estimated Signal

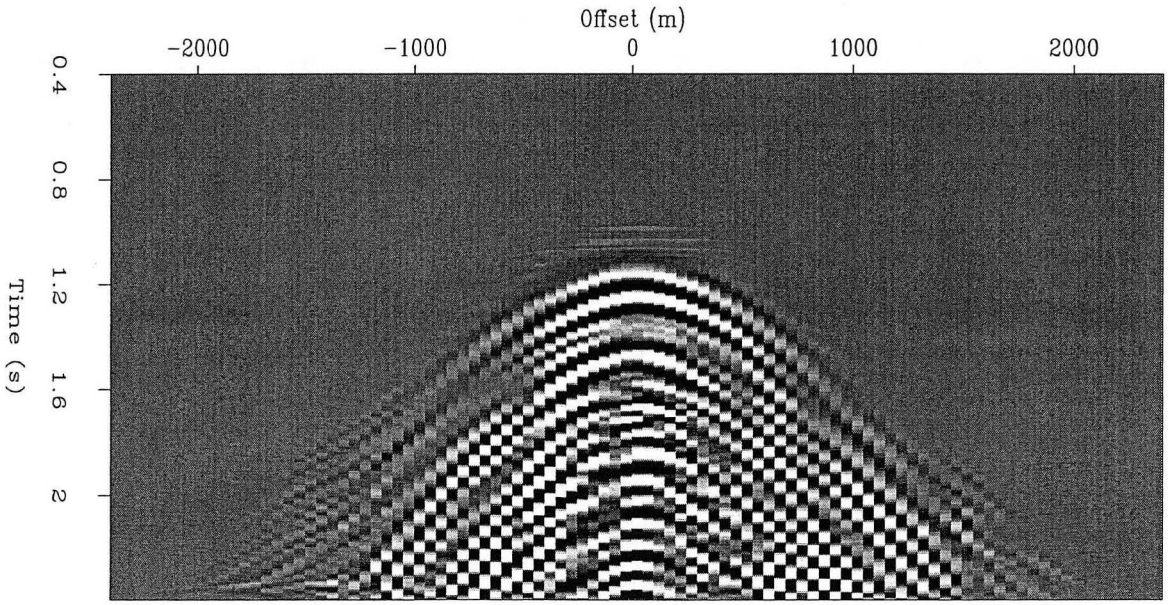

Estimated Noise

Figure 19.

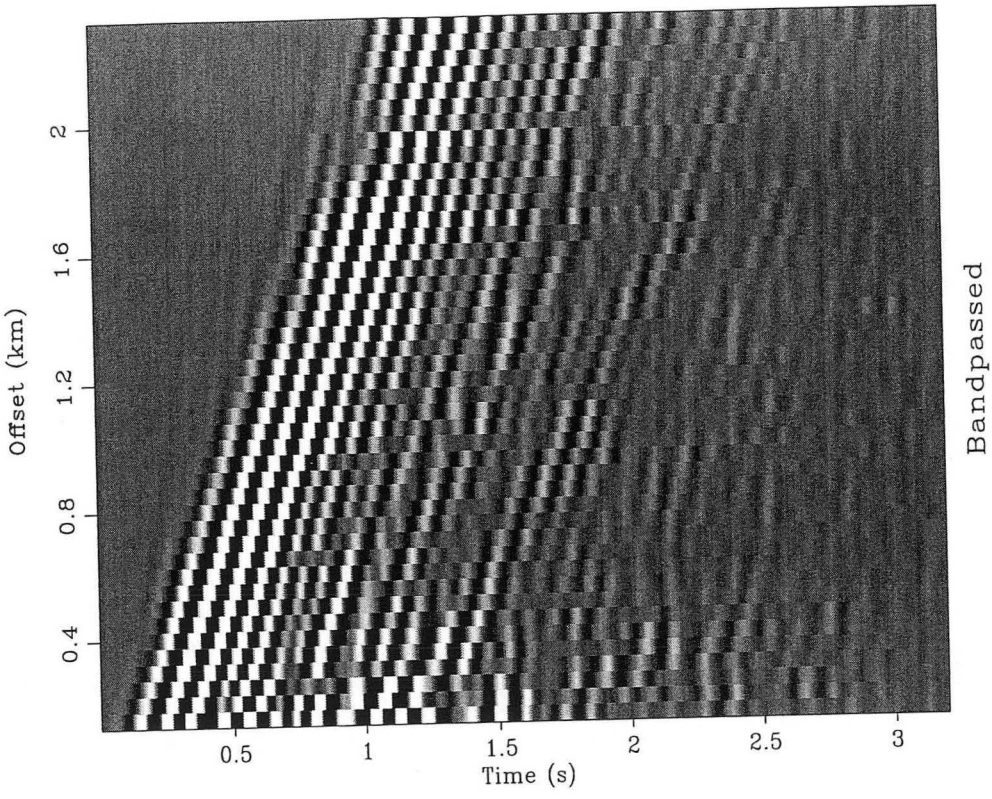
Offset (km)
0.4
0.8
1.2
1.6
2
0.5
1
1.5
2
2.5
3
Time (s)
Bandpassed

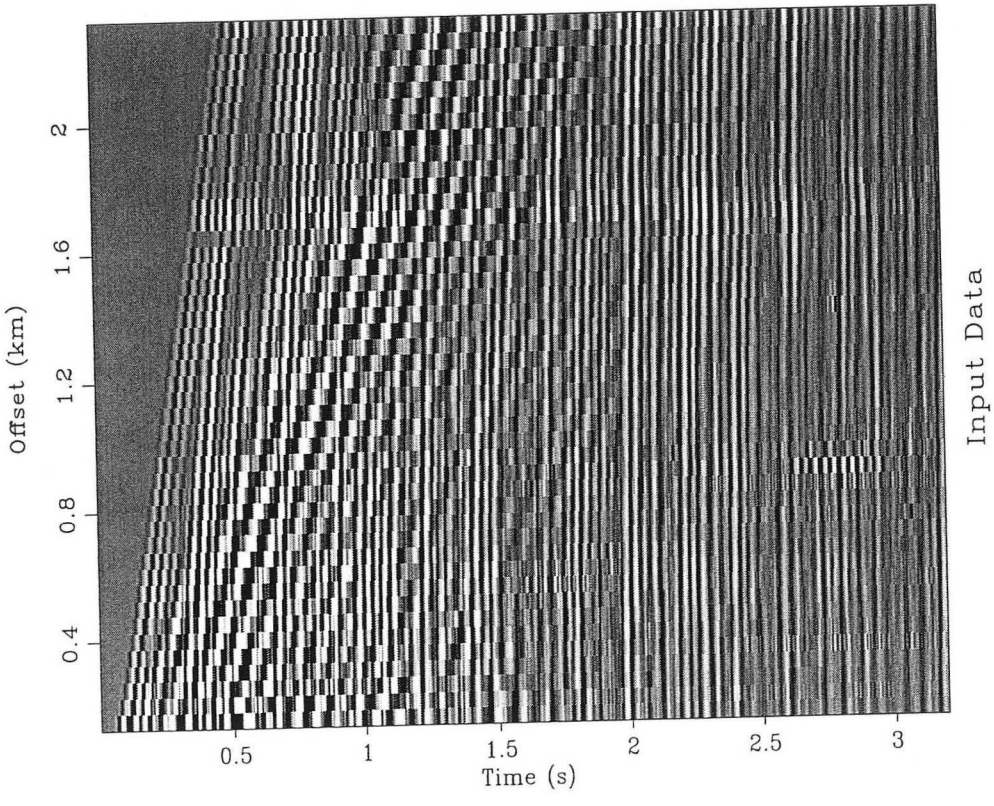
Offset (km)
0.4
0.8
1.2
1.6
2
0.5
1
1.5
2
2.5
3
Time (s)
Input Data

Figure 20.

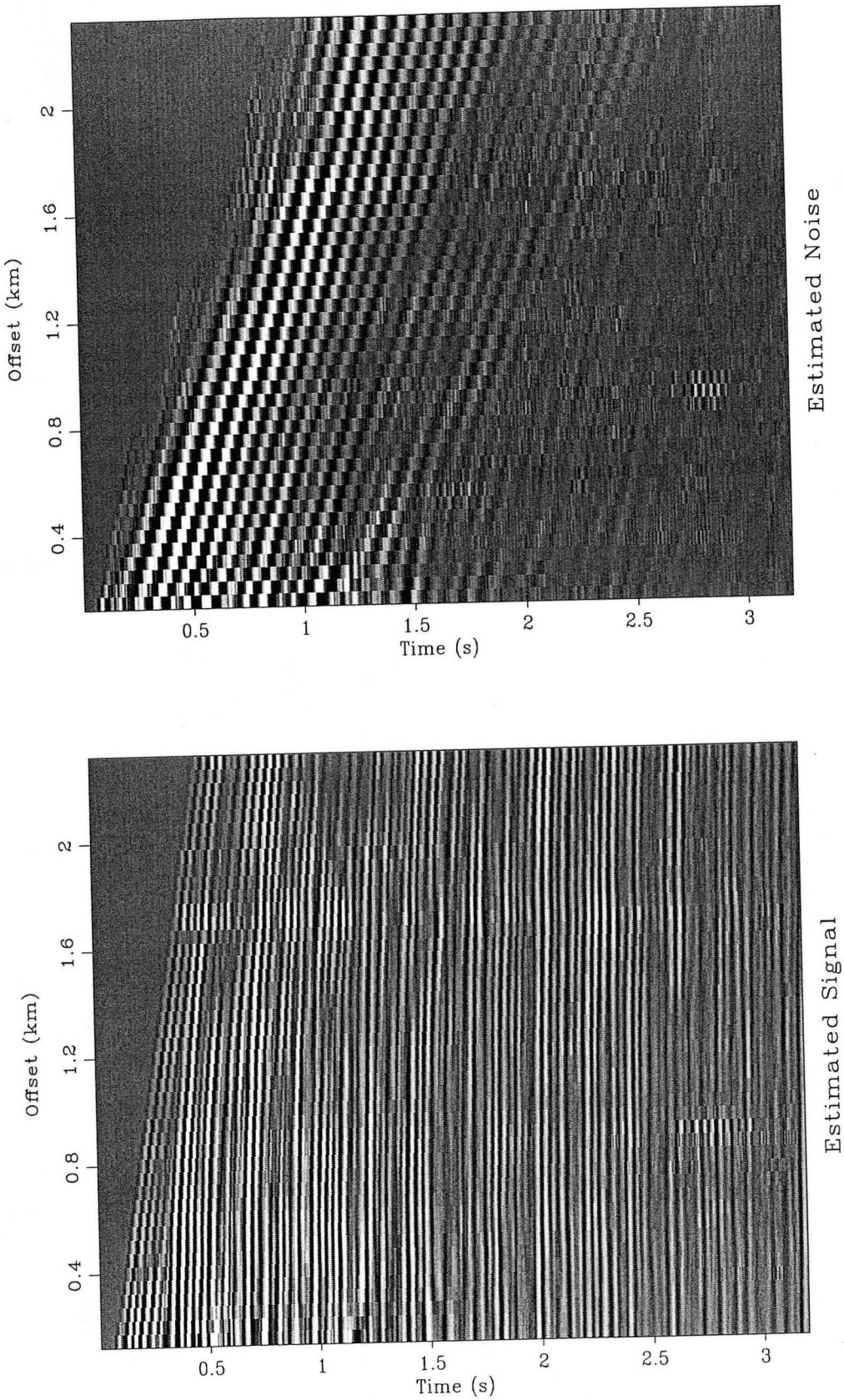
Estimated Noise
Offset (km)
0.4
0.8
1.2
1.6
2
0.5
1
1.5
2
2.5
3
Time (s)
Estimated Signal
Offset (km)
0.4
0.8
1.2
1.6
2
0.5
1
1.5
2
2.5
3
Time (s)

Figure 21.

Ernest Orlando Lawrence Berkeley National Laboratory
One Cyclotron Road | Berkeley, California 94720

Prepared for the U.S. Department of Energy under Contract No. DE-AC03-76SF00098